

Near-field flow characteristics of a free coaxial jet

A. Mitra^a, S. Murugan^b, R. van Hout^{b,*}, A. Kleiman^a, M. Raizner^c, B. Cukurel^a

^a Technion - Israel Institute of Technology, Faculty of Aeronautics, Technion city, Haifa, 3200003, Israel

^b Technion - Israel Institute of Technology, Faculty of Mechanical Engineering, Technion city, Haifa, 3200003, Israel

^c Rafael Advanced Defense Systems, Haifa, 3102102, Israel

ARTICLE INFO

Keywords:

Jet flows

Coaxial jets

Particle image velocimetry (PIV)

Vortex distribution

ABSTRACT

Detailed planar PIV measurements are reported of the flow field in the near-field of a free coaxial air jet. Measurements were performed at outer to inner jet velocity ratios of $r_u (= U_o/U_i) = \infty, 2, 1$, and 0.5 , while keeping U_o constant. Mean velocity distributions and turbulent stress distributions compared well to those reported in the literature at similar r_u . The spatial organization of the generated vortices, analyzed based on the instantaneous vorticity and swirling strength distributions, revealed distinct spatial wavelengths. Associated Strouhal numbers (assuming vortex convection velocities) were higher than those reported in the literature for different nozzle geometries. Our results point at the importance of the nozzle geometry and associated flow exit conditions on the vortex generation frequency. In addition, for the present nozzle geometry and jet exit flow conditions, the outer and inner jet are strongly coupled.

1. Introduction

Jets of varying geometric shapes can be found in a wide variety of industrial applications. One of the simplest, most widely studied geometries is the single round jet that when issued into a quiescent environment will entrain ambient fluid and spread in the radial direction with downstream distance. In this downstream direction, the flow field characteristics differ in the near-field, the intermediate and the far-field. As a result of the high shear, the near-field flow characteristics are governed by Kelvin Helmholtz (K-H) instabilities that lead to the generation of large coherent toroidal vortices (Popiel and Trass, 1991; Raizner et al., 2018; van Hout et al., 2018; Raizner and van Hout, 2020). The K-H instability modes may be axisymmetric or helical (Cohen and Wygnanski, 1987; Michalke, 1984) and their characteristics are important since they drive the near-field mass and momentum transport, thereby affecting the spread of the jet, rate of entrainment and the decay of the axial jet velocity, amongst others. For a comprehensive review of research on single, round turbulent jets, as well as a historical overview, the reader is referred to Ball et al. (2012) and references herein.

A variation on the single round jet is the coaxial, round jet that consists of a central jet (hereafter termed “inner” jet) surrounded by a concentric, annular jet (hereafter termed “outer” jet), schematically depicted in Fig. 1. The exit velocity profiles of the inner and outer jet depend on the geometry of the nozzle. Three boundary layers develop within the nozzle (Fig. 1), one associated with the outer interface of the inner jet (superscript “i”) having a thickness, δ^i , and two associated

with the inner, δ^{io} , and outer, δ^o , interfaces of the outer jet denoted by superscripts “io” and “o”, respectively. For all geometries, a velocity difference between the inner and outer jet exit velocities, U_i and U_o , respectively, leads to a velocity jump resulting in shear layers that develop between the inner and the outer jet. Here, the subscripts “i” and “o” denote inner and outer jet, respectively. In addition, when the jet flows into a quiescent ambient fluid, the velocity jump between U_o and the quiescent ambient creates an outer shear layer. Note that as the outer and inner jet merge downstream of the jet exit, only the outer shear layer remains. Close to the nozzle exit, the shear layers become unstable through K-H instabilities and as a result, an inner mixing region (IMR) separating between the inner and outer jet as well as an outer mixing region (OMR) separating between the outer jet and the ambient, appear (see Fig. 1). The vortices that develop in the inner and outer mixing regions will be termed “primary” and “secondary” vortices, respectively. They may interact with each other in the near-field of the coaxial jet and their kinematics govern the mixing between the inner and the outer jets in this region (Gladnick et al., 1990; Buresti et al., 1998). Note that the strong demand for uniform mixing in many industrial applications such as rocket injectors and industrial burners (Champagne and Wygnanski, 1971), may be achieved by employing coaxial jets. As a result, there is a need for in-depth understanding of the generation and development of the near-field primary and secondary vortices and associated mixing in a coaxial jet.

* Corresponding author.

E-mail address: rene@technion.ac.il (R. van Hout).

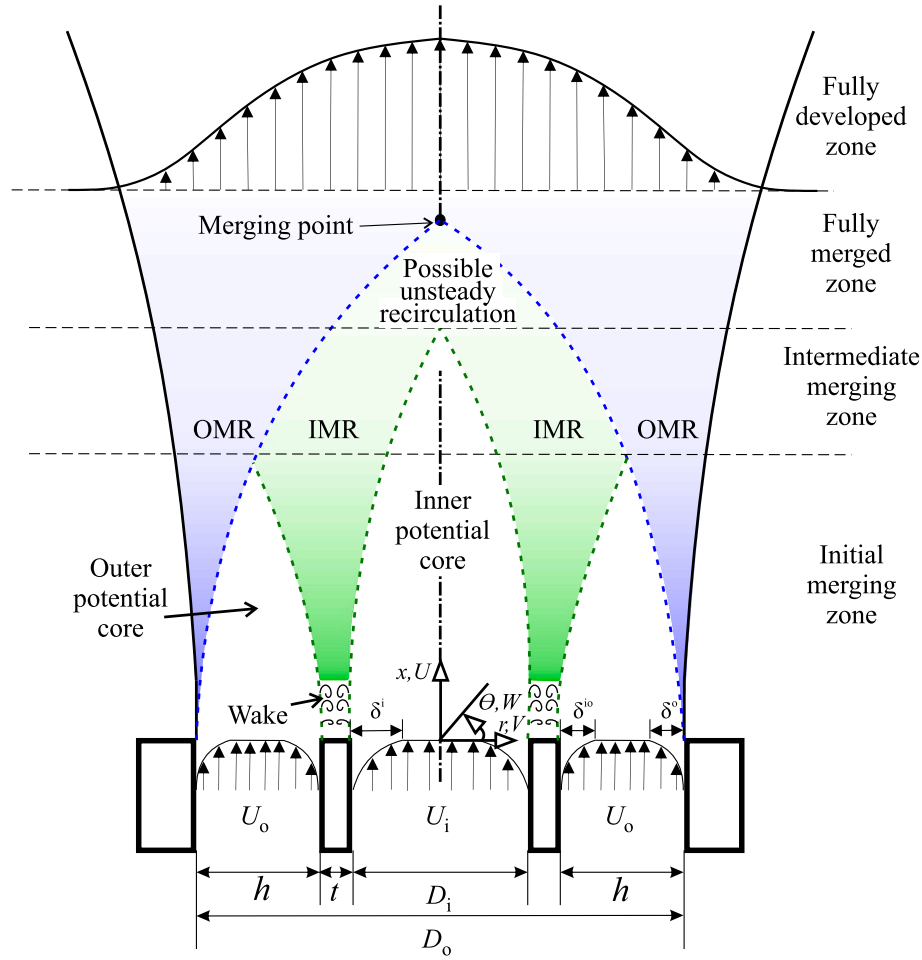


Fig. 1. Schematic representation of the development of the flow field downstream of the jet nozzle including different zones that can be identified. Source: Adapted from van Hout et al. (2021).

Mixing in coaxial jets is primarily controlled by the momentum flux ratio, $M = \rho_o U_o / \rho_i U_i$, where ρ denotes the fluid density. Here, we limit ourselves to same density fluids and in that case M reduces to the velocity ratio, $r_u = U_o / U_i$. In addition to r_u , the geometry of the nozzle as well as its area ratio, A_o / A_i , affect the downstream flow field. Here, $A_o = \frac{\pi}{4} (D_o^2 - (D_i + 2t)^2)$ and $A_i = \frac{\pi}{4} D_i^2$, denote the outer and inner jet exit areas, respectively; D_o and D_i denote the outer and inner jet diameters, respectively. The velocity profiles of the inner and outer jets at the nozzle exit depend on the shape of the nozzle while the finite wall thickness, t , of the inner nozzle (see Fig. 1) may lead to wake instabilities in addition to the aforementioned shear layer instabilities (Segalini and Talamelli, 2011; van Hout et al., 2021). For well-designed contracting nozzles (Champagne and Wygnanski, 1971), jet exit velocities are nearly uniform and are characterized by so-called “top hat” profiles. The potential core length of the inner jet strongly depends on r_u in contrast to that of the outer jet that is set by the diameter ratio, $\beta = D_o / D_i$ (Rehab et al., 1997). For r_u exceeding a critical value (between $r_u = 5$ to 8, depending on the shape of the jet exit velocity profiles), an unsteady recirculation bubble may appear located between the merging point and the end of the inner potential core (Chigier and Beér, 1964; Rehab et al., 1997) (see Fig. 1). Rehab et al. (1997) showed that the instability in the recirculating region is characterized by a low frequency azimuthal mode which contributes to a drastic reduction of the inner potential core length. Next a brief literature review of research pertinent to the present work is presented. For an in-depth overview, the reader is referred to the recent review of coaxial jets by van Hout et al. (2021) and references herein.

Point as well as planar measurement techniques such as hot-wire anemometry, laser doppler velocimetry, microphones, and molecular tagging velocimetry have been used to measure the turbulent flow characteristics and associated static pressure distribution in the near and far field region of the coaxial jet (e.g. Ko and Kwan, 1976; Au and Ko, 1987; Champagne and Wygnanski, 1971; Buresti et al., 1994; Sadr and Klewicki, 2003). Chigier and Beér (1964) reported one of the first detailed measurements of the average flow and pressure fields in the near-field of a coaxial jet at various velocity ratios. A series of experiments using hot wire anemometry by the research group of Ko (Ko and Kwan, 1976; Ko and Au, 1985; Kwan and Ko, 1976; Ko and Au, 1981; Au and Ko, 1987) provided detailed information on the near-field flow characteristics of coaxial jets at various r_u . Based on their results, they concluded that the primary and secondary vortices develop independently like in corresponding single jets. However, in contrast to these results, almost three decades later, Dahm et al. (1992) using flow visualizations, observed that primary and secondary vortices were strongly coupled. This strong dependence results in different interaction dynamics leading to different mixing patterns in the near-field. In agreement with Ko’s research group, such coupling was not observed by Buresti et al. (1994, 1998), possibly because of their larger area ratio.

The near-field of a coaxial jet can be divided into distinct merging zones, i.e. initial, intermediate and fully merged zones (Kwan and Ko, 1976; Ko and Au, 1985), as illustrated in Fig. 1. The relative extent of each of these zones strongly depends on r_u . As r_u is increased from zero (single jet), the elongation factor ‘e’, defined as the ratio of the length of the inner potential core to that of a single, round jet, increases and

reaches a maximum of about 2 for $r_u = 1$ (Champagne and Wygnanski, 1971; Kwan, 1975; Rajaratnam, 1976; Ko and Au, 1981; Au and Ko, 1987; Rehab et al., 1997; van Hout et al., 2021). Dahm et al. (1992) visualized the near field vortical structures in coaxial jets and showed that not only they depend on r_u but also on the absolute velocities of both jets for a given r_u . The mixing properties of one-phase coaxial jets (Villermaux and Rehab, 2000) at $r_u > 1$ were shown to be dictated by the vorticity thickness of the outer jet, and the elongation rate defined as $\gamma = (U_o - U_i)/h$ where h denotes the annular gap width, $h = D_o - (D_i + 2t)$. Villermaux and Rehab (2000) showed that the rate at which the mixture evolves from initial separation towards uniformity is prescribed by γ^{-1} , while the vorticity thickness determines the primary shear instability wavelength.

In the far-field, the turbulent coaxial jet flow becomes fully mixed and reaches self-similarity in the fully developed zone (Fig. 1). Self-similarity is reached faster for a coaxial jet (Duraõ and Whitelaw, 1973) compared to a single jet with the same mass flow rate, due to enhanced mixing (Champagne and Wygnanski, 1971; Duraõ and Whitelaw, 1973; Ribeiro and Whitelaw, 1976). Note that even when $U_i = U_o$ ($r_u = 1$), a coaxial jet develops faster than a single jet because of a strong imbalance between production and dissipation of turbulent kinetic energy in the wake (Fig. 1), which leads to increased mixing compared to a single jet. Note that mixing may be even further enhanced by introducing swirl (Champagne and Kromat, 2000; Kadu et al., 2020). However, this is outside the scope of the present investigation.

In contrast to the large number of experimental studies, relatively few numerical studies on incompressible, swirl-free, circular, coaxial jets of fluids of the same density have been carried out in the last two decades. One of the first large eddy simulation (LES) studies of turbulent, confined coaxial jets motivated by the mixing of a coaxial jet combustion was performed by Akselvoll and Moin (1996). Both LES and direct numerical simulations (DNS) have focused mainly on cases for which $r_u > 2$ (da Silva et al., 2003; Balarac and Métais, 2005; Balarac et al., 2007b,a). These studies indicated that the initial shear layer thickness of the inner nozzle, quantified by its momentum thickness, governs the jet's spreading rate, the size and extent of the recirculating region, the inner and outer potential core lengths, as well as the growth rates of instabilities in the inner and outer shear layers. Instabilities were further studied for unitary velocity ratios ($r_u = 1$) by Canton et al. (2017) and Montagnani and Auteri (2019). They found that coaxial jets are globally unstable at a velocity ratio close to unity when the Reynolds number exceeds about 1350. This is similar to the wake instability observed in the inviscid analysis of Talamelli and Gavarini (2006). Moreover, the flow is subcritically unstable for Reynolds numbers below 1350.

None of the above literature publications has provided detailed quantitative spatial and temporal information on primary and secondary vortex generation and the interaction between them. The goal of the present study is to fill this gap and provide quantitative results on the spatial distribution of primary and secondary vortices, as well as their strength, number and size distributions. In this study, U_o was fixed while U_i was stepwise increased from zero to $U_i = 2U_o$, resulting in $r_u = \infty, 2, 1$, and 0.5 . In this way, the outer shear layer's velocity jump was kept constant at $\Delta U_o = U_o$ while the inner shear layer's velocity jump was constantly changed. The experimental setup including the employed planar particle image velocimetry (PIV) system and data processing are presented in Section 2 after which the mean flow field and turbulence inlet conditions are presented in Section 3. The primary and secondary vortex characteristics are then presented in Section 4 while a short summary and discussion is given in Section 5.

2. Experimental setup and data processing

Experiments were performed using a free coaxial, round jet apparatus schematically depicted in Fig. 2. Compressed air passed through a water separator, a pressure regulator, and a particle filter (5 μm) after

which the air flow was split into two streams, one connected to the inner jet and the other to the outer jet. Each stream passed through a mass flow controller (Alicat, range of 600 SLPM), after which they were separately seeded by two aerosol generators (LaVision GmbH; Aerosol fluid: Di-Ethyl-Hexyl-Sebacat (DEHS), density: $\rho = 0.91 \text{ g/cm}^3$; droplet size $< 1 \mu\text{m}$). The coaxial jet nozzle was custom designed and 3D printed in parts that were bolted together after which it was sealed. The concentricity of the inner and the outer jet was validated by imaging the assembled nozzle exit and using image processing tools (Matlab toolbox). Based on this, the inner jet's diameter was, $D_i = 6 \text{ mm} \pm 0.1 \text{ mm}$, the wall thickness was $t = 1 \pm 0.05 \text{ mm}$, and the outer jet's exit diameter was $D_o = 10 \text{ mm} \pm 0.1 \text{ mm}$. The area ratio was taken as unity, $A_o/A_i = 1$, resulting in an annular gap of $h = 1 \text{ mm} \pm 0.1 \text{ mm}$ (Fig. 2). In order to make sure that a fully turbulent developed velocity profile was obtained at the exit of the inner jet, it was issued from a straight tube having a length of $L = 37 \text{ cm}$ ($L/D_i = 61.7$). After being directed through a volute, the outer jet was issued from a converging nozzle (contraction ratio 3:1). The cross-sectional diameter of the volute was systematically reduced to balance the drop in mass flow rate thereby ensuring axisymmetry of the outer jet exit velocity. Furthermore, guiding vanes at the inlet of the nozzle were used to de-swirl the incoming flow and minimize any azimuthal velocity component. Note that the coaxial jet was issued into a large room and adjacent walls were located at least $150D_o$ away from the nozzle exit. The employed right-handed cylindrical coordinate system with its origin located at the center of the inner jet's nozzle exit is shown in Fig. 2, where r , θ , and x denote the radial, azimuthal and axial directions, respectively; U_r , U_θ , and U_x denote the corresponding instantaneous velocities, while the fluctuating velocities are denoted by u_r , u_θ , and u_x . An overbar represents ensemble averaged values, and root-mean-square (rms) values are indicated by a prime.

A planar particle image velocimetry (PIV) system was used to measure the near-field flow characteristics. The system comprised a pulsed Nd-Yag laser (BigSky, 532 nm, 50mJ/pulse at 15 Hz), a CCD camera (Imager SX 4M, $2,360 \times 1,776$ pixels), laser sheet optics consisting of two spherical lenses and a cylindrical lens, as well as data acquisition and processing software (LaVision GmbH, DaVis10). The laser sheet had a thickness of 0.5 mm and was vertically aligned along the center axis of the coaxial jet. The PIV system was operated in dual-frame mode and the laser pulse-delay between the first and the second pulse was chosen such that the maximum pixel displacement of the tracer particles was approximately 10 pixels. The camera was equipped with a 105 mm lens (Nikon, Micro-Nikkor) resulting in a field of view (FOV) of $3.4D_o \times 4.7D_o$ (length \times width) extending from the nozzle exit in the downstream direction. Experiments were performed at several decreasing velocity ratios, $r_u = \infty, 2, 1$, and 0.5 , achieved by keeping U_o constant, $U_o = 29.37 \pm 0.06 \text{ m/s}$, while increasing U_i . As a result, the velocity jump of the outer shear layer, i.e. between the outer jet and the ambient is constant, $\Delta U_o = U_o$, while the velocity jump in the inner shear layer, $\Delta U_i = U_o - U_i$, changes with r_u . As U_i is increased, ΔU_i reduces and becomes negative for $r_u = 0.5$. Further note that for $r_u = 1$, $\Delta U_i = 0$ and only wake instabilities as a result of the finite pipe wall thickness (Fig. 1) are expected to play a role close to the nozzle exit. In addition, the case where $r_u = 0$ (inner jet only) was measured as reference case.

Data sets of 3000 independent pairs of PIV images were acquired at 15 Hz for each r_u . Velocity vectors were determined by a multi-pass cross-correlation algorithm (as implemented in DaVis 10) with an initial interrogation window size of 48×48 pixels that was reduced in the final step to 32×32 pixels with 50% overlap resulting in a vector spacing of 0.32 mm and a spatial resolution of 0.64 mm. Note that the limited spatial resolution acts as a low-pass filter. In order to remove spurious vectors, vector post-processing was applied, including robust outlier removal (Westerweel and Scarano, 2005) after which the removed vectors were replaced by interpolation and the resulting vector maps were smoothed using a Gaussian kernel (as implemented in DaVis

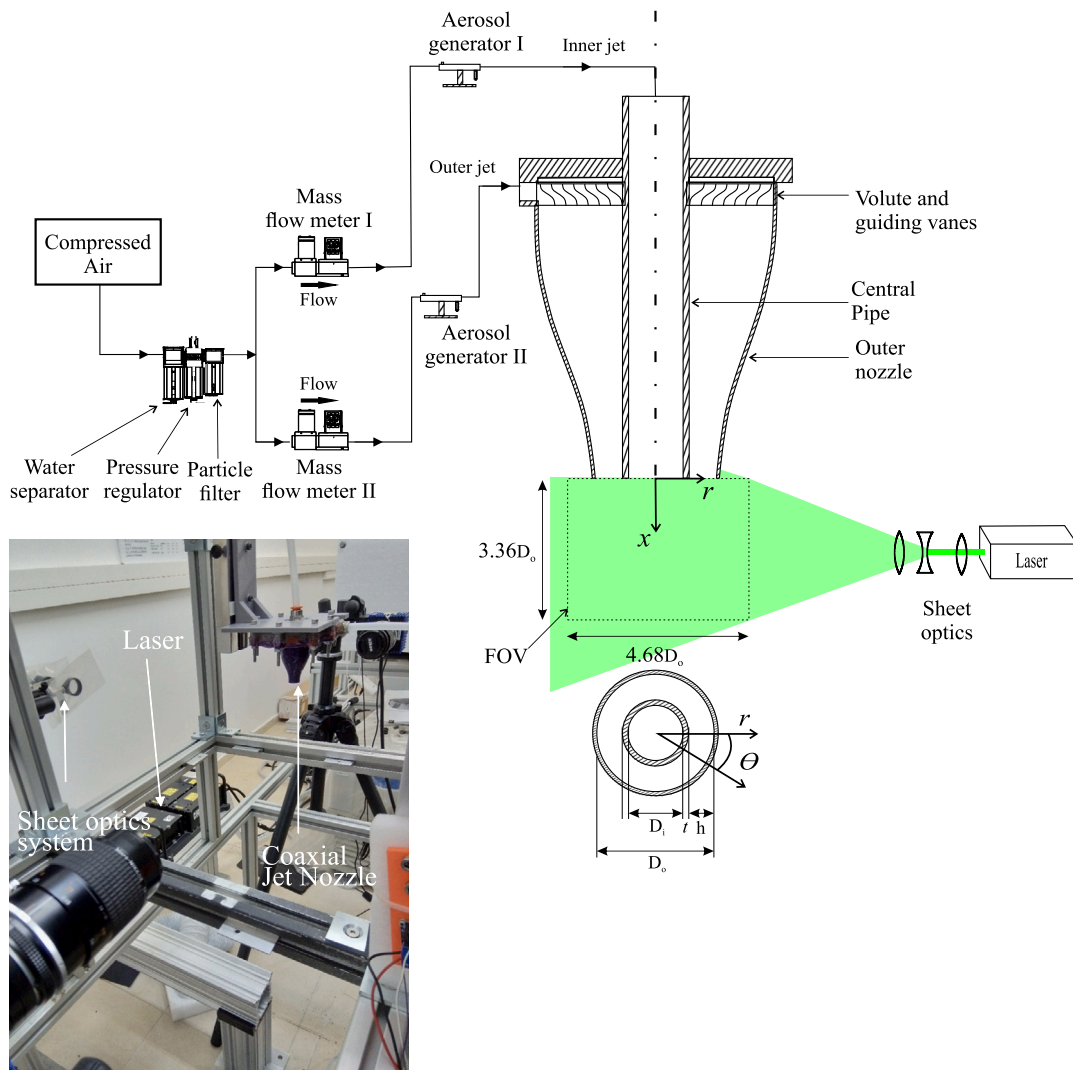


Fig. 2. Schematic layout and actual picture of the experimental setup (not to scale).

10). The statistical measurement uncertainties (not including effects of limited spatial resolution) were evaluated under the assumption of uncorrelated and normally distributed velocities (Benedict and Gould, 1996). Under these constraints and for a 95% confidence interval, the uncertainties of the maximum ensemble averaged velocities, Reynolds normal stresses, and Reynolds shear stresses, did not exceed $\pm 0.6\%$, $\pm 3.6\%$, and $\pm 14\%$, respectively.

In order to visualize instantaneous vortical structures and shear layers, both the out-of-plane vorticity (hereafter termed “vorticity”), $\omega = (\partial U_r / \partial x - \partial U_x / \partial r)$, and the directional swirling strength, $\Lambda_{ci} = \lambda_{ci} \omega / |\omega|$ (Adrian et al., 2000; van Hout et al., 2013, 2018; Raizner et al., 2019b) were used. Here, the swirling strength, λ_{ci} , denotes the complex imaginary eigenvector of the velocity gradient tensor evaluated for a 2D vector field. The spatial velocity gradients were determined based on a central difference scheme. Note that while the vorticity displays both shear layers and rotational motion, the Galilean invariant swirling strength isolates rotational motion and is preferred over reference frame dependent vector maps for the visualization of vortices (Adrian et al., 2000; Raizner et al., 2019a). Further note that as a result of the limited spatial resolution, flow structures of scales smaller than $0.06 D_0$ cannot be detected in the present data sets (Adrian and Westerweel, 2011) while the magnitudes of the velocity gradients and the determined vorticity and swirling strength were underestimated. However, since in the present analysis the latter two were mostly used as vortex

identifiers (see Section 4), accurate values are less important (Raizner and van Hout, 2020).

An example of the employed methodology and its result is depicted in typical vorticity and swirling strength snapshots shown in Fig. 3 for $r_u = 2$. Comparing the instantaneous vorticity and swirling strength distributions in Figs. 3a and b, respectively, it is clearly observed that the swirling strength detects most of the high vorticity blobs that can be associated with swirl motion (Zhou et al., 1999; Chakraborty et al., 2005). Since the strength of the vortices decreases with increasing distance from the nozzle, as well as to remove spurious data, distributions of Λ_{ci} were high-pass filtered by a threshold value based on the local (function of x) rms value of the computed swirling strengths, $C \Lambda'_{ci}(x)$. C was taken as 0.6 after it was verified that no relevant data was removed. Subsequently, the resulting instantaneous swirling strength distributions were binarized and using Matlab’s “blob” analysis, the size and centroid positions of the detected blobs were determined. Detected centroids of positive (hereafter denoted by “+ve”) and negative (hereafter denoted by “-ve”) swirling strength “blobs” are indicated in Fig. 3b by “+” and “x” symbols, respectively. Note that these blobs represent cross-sections of three-dimensional vortical structures and especially close to the nozzle exit, it can be observed that symmetric about $r/D = 0$, “blobs” align well and pairs (1,2), (3,4) and (5,6) are likely the cross-sections of large toroidal vortices that are known to be generated as a result of K-H instabilities (Violato et al., 2012).

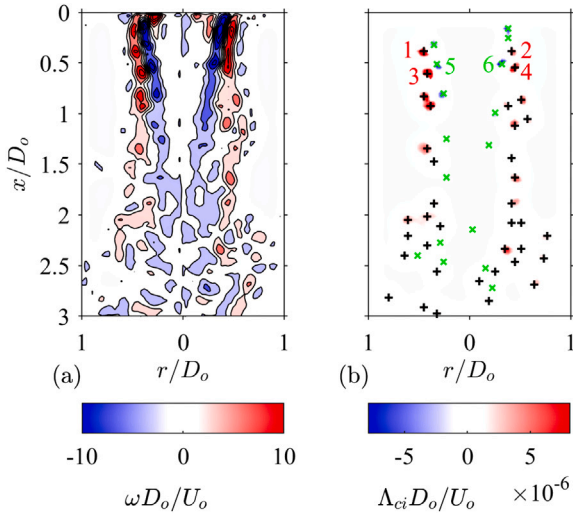


Fig. 3. Example snapshot contour plots ($r_u = 2.0$) of (a) the vorticity, and (b) the swirling strength. Black “+” and green “x” symbols in (b) denote the detected vortex centroid positions of +ve and -ve sign vortices, respectively. (For interpretation of the references to color in this figure legend, the reader is referred to the web version of this article.)

Farther downstream, these large-scale toroidal vortices break up and many more weaker “signatures” of vortical structures can be observed. The identified swirling strength blobs were used to determine their circulation by integrating the vorticity over its area, $\Gamma = \int_A \omega dA$, where A denotes the detected cross-sectional area of the blob.

3. Results

3.1. Mean velocity distributions

Contour plots of the ensemble averaged, normalized axial and radial velocities are depicted in the left and right columns of Fig. 4, respectively, for $r_u = \infty, 2, 1$, and 0.5 . Accompanying values of the normalized jet’s half width, $r_{1/2}/D_o$, and normalized axial velocity at the jet’s centerline ($r/D_o = 0$), \bar{U}_x^c/U_o ($r_u = \infty, 2, 1, 0.5$) and \bar{U}_x/U_i ($r_u = 0$), are shown as a function of x/D_o in Fig. 5 together with data taken from Ko and Au (1981), where the superscript “c” denotes “at the jet’s centerline”. The jet’s half width is defined here as the radial location where locally, downstream of the nozzle, $\bar{U}_x(x, r)$ equals half the local, maximum jet velocity, \bar{U}_x^{max} which may be off-axis for a coaxial jet in contrast to a single round jet. Furthermore, for an annular jet, this definition may result in multiple radial locations for which $\bar{U}_x(x, r) = \bar{U}_x^{max}/2$. In case this occurred, the largest value of $r_{1/2}$ was taken as the halfwidth.

For an annular jet, Chigier and Beér (1964) showed that close to the nozzle exit a recirculating toroidal vortex exists similar as in the present case ($r_u = \infty$, Figs. 4a,b), where the distribution of \bar{U}_x/U_o (Fig. 4a) and the change of $r_{1/2}/D_o$ with x/D_o (Fig. 5a), indicate a “contraction” of the jet. Associated with this recirculating vortex is a zone of sub-atmospheric pressure resulting in a radially inward directed pressure that draws the annular jet towards the jet axis. Values of $r_{1/2}/D_o$ display a minimum at $x/D_o \approx 1.1$ ($r_{1/2}/D_o \approx 0.34$) after which they increase and reach $r_{1/2}/D_o \approx 0.4$ at $x/D_o \approx 3$. Associated values of \bar{U}_x^c/U_o (Fig. 5b) are negative close to the nozzle exit and cross zero (stagnation point) at $x/D_o \approx 0.73$, i.e. just before $r_{1/2}/D_o$ reaches its minimum value.

Introducing the inner jet, $U_i = U_o/2$ ($r_u = 2$), dramatically changes the mean flow pattern as observed in Figs. 4c, d. The strong inward directed \bar{U}_r , close to the nozzle exit for $r_u = \infty$ (Fig. 4b) mostly disappears (Fig. 4d) and jet contraction is small as illustrated by the

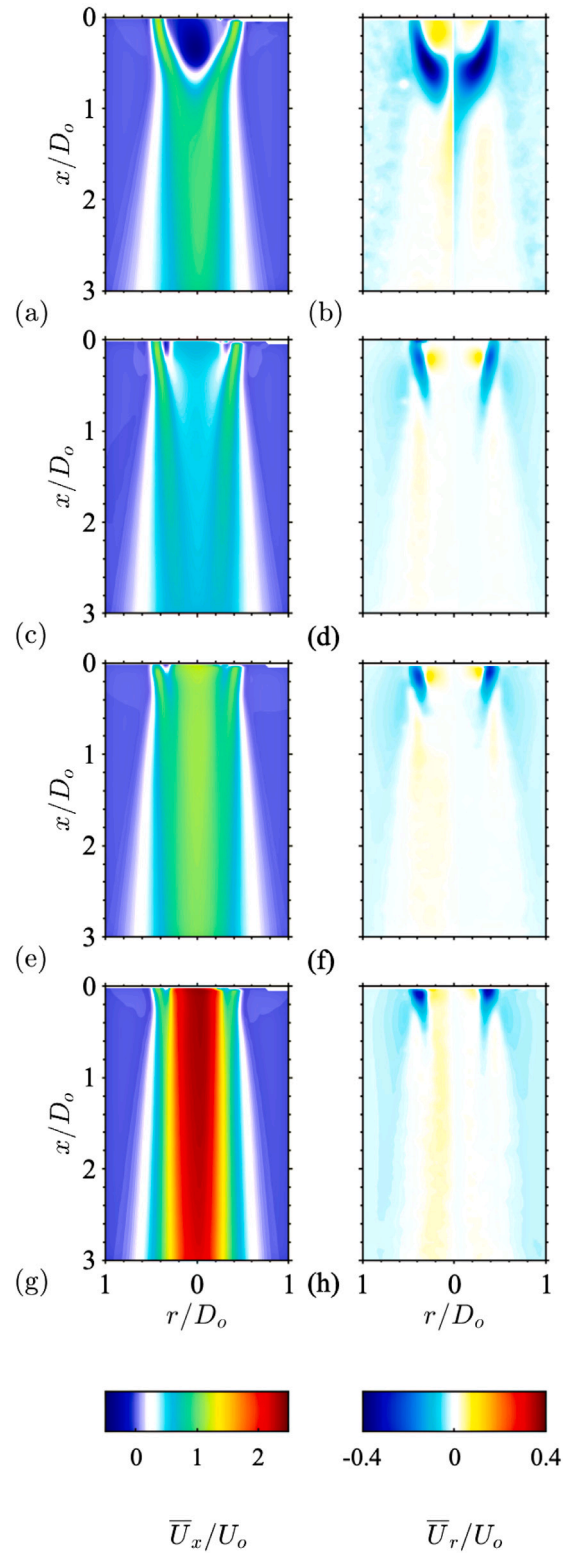


Fig. 4. Contour plots of the ensemble averaged, axial (left column) and radial (right column) jet velocity normalized by the outer jet exit velocity for $r_u =$ (a, b) ∞ , (c, d) 2, (e, f) 1, and (g, h) 0.5.

change of $r_{1/2}/D_o$ with x/D_o depicted in Fig. 5a. Although the profiles of $r_{1/2}/D_o$ have similar shapes for both $r_u = \infty$ and 2, values of $r_{1/2}/D_o$ for $r_u = 2$ exceed those for $r_u = \infty$ within the measurement range. As r_u is further reduced to $r_u = 1.0$, the local minima of $r_{1/2}/D_o$ decrease

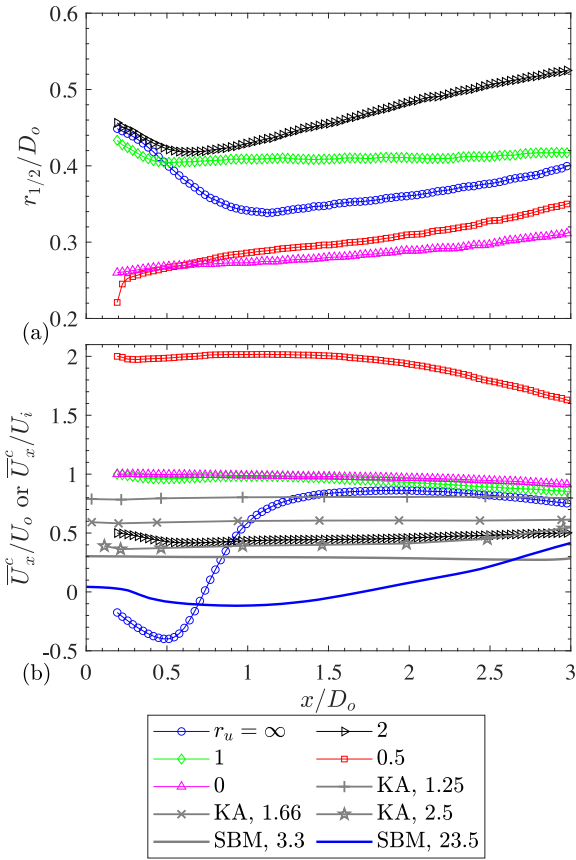


Fig. 5. Axial profiles of the normalized (a) jet's half width, and (b) axial centerline velocity. Uncertainties based on 95% confidence intervals did not exceed $\pm 0.6\%$. “KA” and “SBM” indicate data taken from Figs. 2 (Ko and Au, 1981) and 5 (da Silva et al., 2003), respectively. Note that normalization in (b) is by U_i for $r_u = 0$, and by U_o in all other cases. Legend numbers denote r_u values.

compared to $r_u = 2$ (Fig. 5a). The jet still slightly contracts (up to $x/D_o \approx 0.54$, Figs. 4e,f and 5a) but beyond $x/D_o \approx 0.54$, $r_{1/2}/D_o$ remains almost constant ($r_{1/2}/D_o \approx 0.41$). Further reducing r_u to 0.5 (Figs. 4g,h), strongly decreases $r_{1/2}/D_o$ (Fig. 5a) as the coaxial jet becomes governed by the inner jet. As illustrated in Fig. 5a, for $r_u = 0.5$, the axial dependence of $r_{1/2}/D_o$ resembles that of a single round jet ($r_u = 0$) at the same U_i . However, for $x/D_o > 0.5$, values of $r_{1/2}/D_o$ for $r_u = 0.5$ exceed those for $r_u = 0$ and increase faster with increasing x/D_o . Furthermore, as the inner jet gains importance, profiles of \bar{U}_x/U_o ($r_u = 1, 0.5$) and \bar{U}_x/U_i ($r_u = 0$) nearly collapse (Fig. 5b) up till $x/D_o \approx 2.2$ indicating a faster decrease in \bar{U}_x/U_o for $r_u = 0.5$ (compared to $r_u = 0$) when $x/D_o > 2.2$, likely as a result of enhanced mixing. The present axial profiles of \bar{U}_x/U_o are compared in Fig. 5b to the measurements reported by Ko and Au (1981) and the DNS results by da Silva et al. (2003). In agreement with the present results, their axial profiles of \bar{U}_x/U_o are flat for $1 \leq r_u \leq 3.3$, with a small reduction of \bar{U}_x/U_o close to the nozzle exit for $r_u = 2.5$ (Ko and Au, 1981), similar as the present results for $r_u = 2$ (Fig. 5b). A clear decrease in \bar{U}_x/U_o can be seen at $r_u = 23.5$ (da Silva et al., 2003) with negative values of \bar{U}_x/U_o (Fig. 5b). However, the difference with the annular case ($r_u = \infty$) is notable and indicates that even at $r_u = 23.5$, the weak inner jet strongly affects the near-field velocity distribution. For example, the stagnation point for $r_u = \infty$ is located at $x/D_o = 0.73$ while it is located at $x/D_o = 1.5$ for $r_u = 23.5$ (da Silva et al., 2003). Note that it may be expected that the stagnation point moves closer to the nozzle as $r_u \rightarrow \infty$ and the effect of the inner jet is removed. Further note that the overall axial variation of \bar{U}_x/U_o and $r_{1/2}/D_o$ is similar to that reported by Chigier and Beér

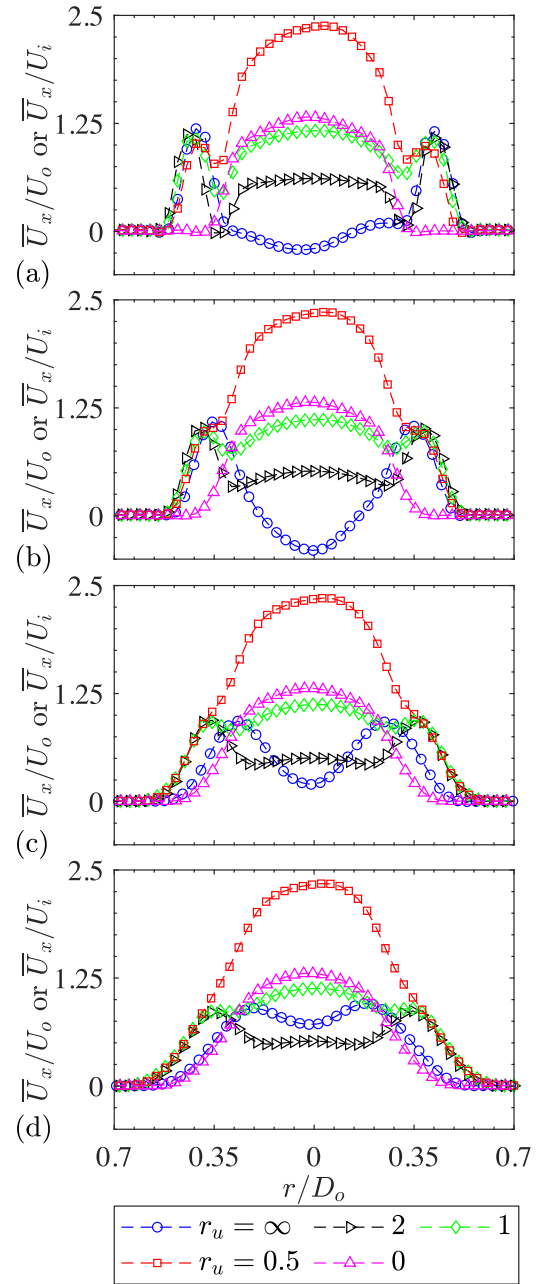


Fig. 6. Radial profiles of the normalized axial velocity for different values of r_u and at different downstream distances from the nozzle exit. $x/D_o =$ (a) 0.25, (b) 0.5, (c) 0.75, and (d) 1.0. Uncertainties based on 95% confidence intervals did not exceed $\pm 0.6\%$. Note that normalization of \bar{U}_x is by U_i for $r_u = 0$, and by U_o in all other cases.

(1964), despite the different geometry of the nozzle. In particular t was significantly larger than in the present study.

In the present research we are interested in the generation of vortices by K-H instabilities in the near-field of the coaxial jet, and it is therefore of interest to look in more detail at the radial profiles of the mean streamwise velocity for different r_u . Profiles of \bar{U}_x/U_o extracted from the contour plots (Fig. 4) are depicted in Fig. 6 at $x/D_o = 0.25, 0.5, 0.75$, and 1.0 . For comparison, profiles for a single jet ($r_u = 0$, \bar{U}_x/U_i) are also displayed. As can be seen, in all cases, the radial profiles are symmetric about $r/D_o = 0$ with some small asymmetries for $r_u = \infty$ close to the inner jet's exit (Fig. 6a) and for $r_u = 0.5$. These are most likely the result of small deficiencies in concentricity between the outer and inner jet as discussed in Section 2.

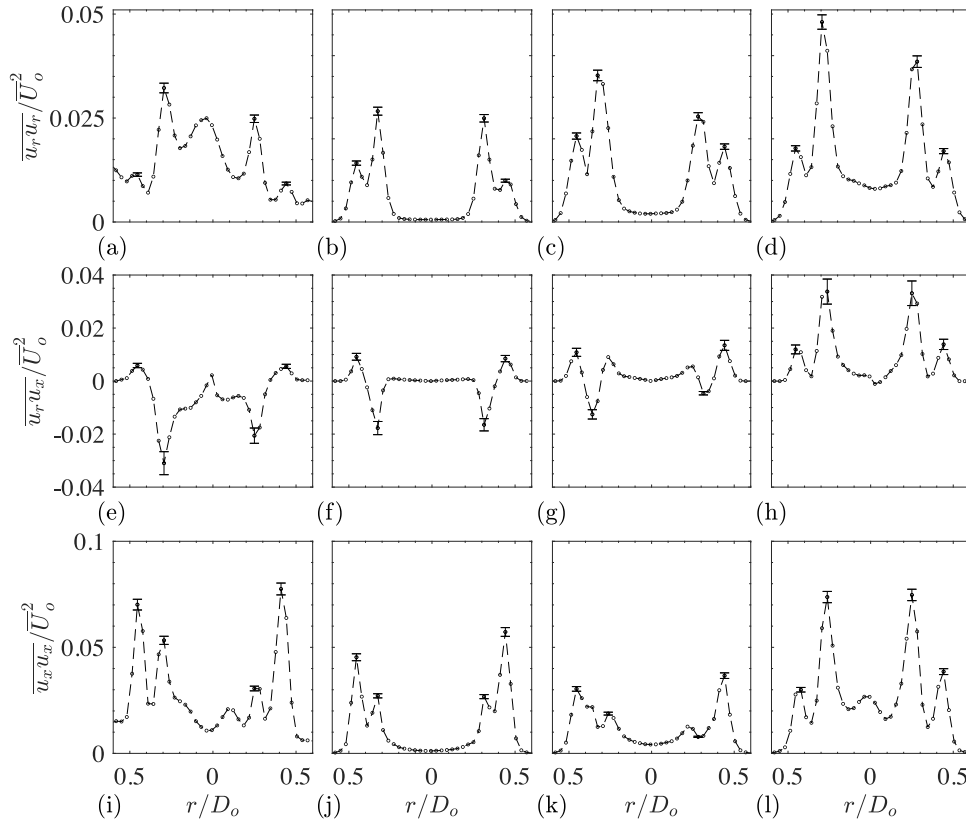


Fig. 7. Radial distributions of the normalized Reynolds stresses at the jet's exit ($x/D_o = 0.5$). (a–d) $\overline{u_r u_r}/U_o^2$, (e–h) $\overline{u_r u_x}/U_o^2$, (i–l) $\overline{u_x u_x}/U_o^2$. $r_u = \infty$ (left column), 2 (2nd column), 1 (3rd column), 0.5 (right column). Representative error bars denote 95% uncertainty bounds.

The radial profiles of $\overline{U_x}/U_o$ for $r_u = 1$ are flattened compared to those of $r_u = 0$ ($\overline{U_x}/U_i$). Since the mass flow rate of the inner jet was the same in both cases, the flattened inner jet's exit velocity profile for $r_u = 1$ must be the result of increased mixing and different pressure distribution due to the presence of the outer jet. Flattening of the inner jet's exit velocity profile becomes more distinct for $r_u = 2$ at $x/D_o = 0.25$ (Fig. 6a). As expected, the lower r_u the lesser the effect of the outer jet and flattening is reduced.

In all cases, outer jet exit velocity profiles at $x/D_o = 0.25$ (between $0.4 < |r/D_o| < 0.5$, Fig. 6a) are strongly peaked with peak values ranging between $1 \leq \overline{U_x}/U_o \leq 1.2$. In agreement with jet contraction (Fig. 5a), radial peak locations move slightly inwards towards the jet axis, mostly so for the annular jet ($r_u = \infty$) that displays the largest contraction (Fig. 5a). The decrease in peak values is similar for all r_u in agreement with the observation that the potential core length of the outer jet is set by β (Rehab et al., 1997). However, with decreasing r_u , the outer and inner jets merge quicker. For example, at $r_u = 0.5$, the inner jet governs the downstream development and the outer jet is almost completely merged with the inner jet at $x/D_o = 0.75$ (Fig. 6c). Note that the general shape of the radial profiles of the streamwise velocity are similar to those reported in other published studies (e.g. Chigier and Beér, 1964; Ribeiro and Whitelaw, 1980).

Note that at the exit, the streamwise velocity distribution is dictated by the three boundary layers that develop within the nozzle (Fig. 1, Segalini and Talamelli, 2011), and in order to characterize the flow conditions at the nozzle exit, we estimated the displacement and momentum thicknesses, $\delta_* = \int_{r_1}^{r_2} \left(1 - \frac{\overline{U_x}}{U}\right) dr$, and $\theta = \int_{r_1}^{r_2} \frac{\overline{U_x}}{U} \left(1 - \frac{\overline{U_x}}{U}\right) dr$, respectively, for each boundary layer based on the profiles of $\overline{U_x}/U_o(r/D_o)$ at $x/D_o = 0.2$. The integration boundaries r_1 and r_2 were taken as the radial positions of minimum and maximum $\overline{U_x}$. The reference velocity U equals U_i and U_o for the boundary layers

associated with the inner and the outer jet, respectively. As a result of the limited spatial measurement resolution, results are only reported for δ^i ($r_u = 0.5$ and 1) and δ^o . Likewise, the vorticity thickness, $\delta_\omega = \Delta U / \left(\partial \overline{U_x} / \partial r\right)^{max}$, was estimated. The determined normalized values of δ_* , θ , and δ_ω as well as the shape factor, $H = \delta_*/\theta$ are summarized in Table 1 together with the associated Reynolds numbers based on the momentum thickness, Re_θ . As expected, the estimated shape factors for the inner layer, H^i , are close to those obtained for turbulent boundary layers (Schlichting and Kestin, 1961) while those for the outer layer are much higher. In addition, it can be seen that for all cases, δ_ω is of the order of the gap thickness, i.e. $h \sim 0.1 D_o$, indicating that we may expect interaction between the inner and outer shear layers (Rehab et al., 1997).

Finally, the radial distributions of the normalized Reynolds normal stresses, $\overline{u_r u_r}/U_o^2$ and $\overline{u_x u_x}/U_o^2$, and shear stresses, $\overline{u_r u_x}/U_o^2$, at the nozzle exit ($x/D_o \approx 0.5$) are depicted in Fig. 7 for all r_u . It can be seen that distributions are not perfectly symmetric about $r/D_o = 0$ which is due to small (within manufacturing accuracy) eccentricity of the nozzle as well as due to limited spatial measurement resolution within the thin shear layers at this measurement position. In all cases, Reynolds stresses are highest away from the jet center ($0.3 < |r/D_o| < 0.5$) and in most cases peaks can be associated with the shear layers just downstream of the nozzle exit. The normal stresses at the inner jet's center are negligible for $r_u = 2$ (Figs. 7b, j) but values increase with decreasing r_u as U_i is increased. Note that the positions of the obtained maxima of $\overline{u_x u_x}/U_o^2$ compare well to those of the maximum turbulence intensity reported by Ko and Au (1985) for $1.25 \leq r_u \leq 6.7$. Further note that peak values of $\overline{u_x u_x}/U_o^2$ are higher than those reported by Au and Ko (1987) ($1.25 \leq r_u \leq 6.7$ at $x/D_o = 1$) who used a well-profiled, contracting nozzle.

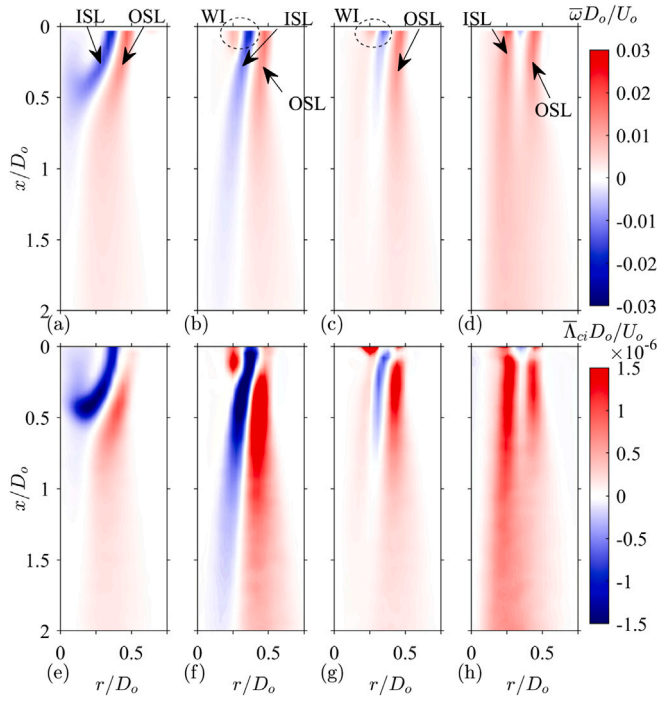


Fig. 8. Contour plots of the normalized, ensemble averaged vorticity (upper row) and swirling strength (bottom row) for different $r_u =$ (a, e) ∞ , (b, f) 2, (c, g) 1, and (d, h) 0.5.

Table 1

Summary of the displacement, momentum, and vorticity thicknesses as well as the shape factors and the Reynolds numbers based on the momentum thickness at the exit of the jet nozzle ($x/D_o \approx 0.2$). Typical estimated uncertainties did not exceed 10%.

r_u	0.5	1	2	∞
δ_s^*/D_o	0.07	0.052		
δ_o^*/D_o	0.067	0.065	0.083	0.056
θ^i/D_o	0.037	0.039		
θ^o/D_o	0.030	0.027	0.028	0.025
H^i	1.89	1.33		
H^o	2.23	2.41	2.96	2.24
Re_{θ^i}	1449	764		
Re_{θ^o}	587	529	548	490
δ_s^i/D_o	0.12	0.11		
δ_o^o/D_o	0.085	0.083	0.078	0.074

4. Primary and secondary vortices

4.1. Ensemble averaged vorticity and swirling strength

It is clear from the above that the near-field region of the coaxial jet is characterized by a spatially changing velocity field with strong shear layers that are expected to govern the downstream structure of the generated jet. The shear layers are better visualized by the out-of-plane component of the vorticity whose normalized, ensemble averaged values, $\bar{\omega}D_o/U_o$, are depicted in the upper row of Fig. 8 for $r_u = \infty$, 2, 1, and 0.5. Note that since the distributions are symmetric about $r/D = 0$, only data for $r/D \geq 0$ are shown. Distinct, opposite sign vorticity layers (red and blue areas in the upper rows of Fig. 8), the result of high shear and vortex generation, are observed in the near-field of the coaxial jet. Their downstream extent depends on r_u . For $r_u = \infty$ (Fig. 8a), an inner shear layer (ISL) generated as a result of the velocity difference between the recirculating region and the outer

jet, is strongly directed inwards towards the jet's centerline. The ISL does not extend much beyond $x/D_o \approx 1$, whereas the outer shear layer (OSL) between the outer jet and the ambient quiescent fluid, extends all the way downstream. Upon introducing the inner jet ($r_u = 2$, Fig. 8b), the annular jet's contraction lessens as a result of the changed pressure distribution (Chigier and Beér, 1964) and both inner and outer shear layers extend downstream across the present field of view. In the close vicinity of the nozzle, signs of wake instability (WI) can be clearly seen as opposite sign vorticity layers depicted within the dashed ellipses in Figs. 8b, c. Note that for $r_u = 1$ (Fig. 8c), $\Delta U_i = 0$, and wake instabilities govern the inner mixing region. However, as can be observed (Fig. 8c), the mean vorticity traces of the wake instability at $r_u = 1$ weaken fast and do not extend much beyond $x/D_o \approx 0.75$ as the velocity deficit decreases (Fig. 6) and velocity gradients become small. For $r_u = 0.5$ (Fig. 8d), ΔU_i changes sign and becomes positive, i.e. $\Delta U_i = \Delta U_o = U_o$. In this case, the inner shear layer is more pronounced than the outer one and extends farther downstream suggesting that mixing in the inner mixing region is reduced compared to that in the outer one at this r_u . Vorticity patterns induced by wake instabilities are weak for this r_u ($= 0.5$).

The identified shear layers in the contour plots of $\bar{\omega}D_o/U_o$ are the result of high, instantaneous shear as well as the generated vortices due to K-H instabilities. These vortices can be seen “embedded” in the example snapshot of the normalized instantaneous vorticity, $\omega D_o/U_o$, depicted in Fig. 3 for $r_u = 2$. As expected from the mean vorticity distribution (Fig. 8), the spatial patterns of $\omega D_o/U_o$ strongly depend on r_u as will be further discussed in Section 4.3. In order to extract the properties of the “embedded” vortices, the instantaneous swirling strength can be used as outlined in Section 2 (Fig. 3b). Such instantaneous swirling strength distributions were determined for all r_u (see also Section 4.3) and their ensemble averaged distributions are depicted in the bottom row of Fig. 8. Note that these complement the ensemble averaged vorticity and provide in an average sense information on the most likely vortex core locations.

The first striking observation is that although the velocity jump $\Delta U_o = U_o$ is constant for all cases and the mean vorticity layer of the OSL looks quite similar (upper row in Fig. 8), changing r_u has a considerable effect on the generated vortices in the OSL, as indicated by the changing spatial patterns of $\bar{\Lambda}_{ci}D_o/U_o$ in the OSL for the different r_u . This indicates that the inner and the outer layer do not develop independently and are coupled in agreement with Dahm et al. (1992) that used a nozzle having a similar area ratio as the one used in the present research, i.e. $A_r \approx 1$. Note that other studies using nozzles with larger A_r (≥ 3 , Ko and Kwan, 1976; Buresti et al., 1994; Wicker and Eaton, 1994) found that the initial vortex development in the ISL and OSL occurs independently in the first few diameters downstream of the nozzle exit. Furthermore, as mentioned by Villermaux and Rehaab (2000), when δ_o at the nozzle exit is not negligibly small compared to h ($= 0.1D_o$), the inner and outer shear layers will interact, resulting in complex vorticity dynamics. In the present case, $\delta_o \sim h$ (see Table 1) and interaction between the inner and outer shear layers is expected to occur.

The ensemble averaged swirling strength distributions indicate where strong, highly coherent vortices reside. For example, it is clear that for $r_u = \infty$ (Fig. 8e), $-ve$ sign vortices hardly leave the recirculation region. They are generated closer to the nozzle exit than the $+ve$ ones in the outer layer that are most prominent at about $x/D_o = 0.5$. For $r_u = 2$ (Fig. 8f), the recirculating wake disappears and $-ve$ sign vortices are advected downstream as indicated by the negative trace of $\bar{\Lambda}_{ci}D_o/U_o$ extending downstream and slightly inwards. Interestingly, near to the nozzle exit ($r/D_o \approx 0.3$, Fig. 8f), a small patch of $+ve$ sign $\bar{\Lambda}_{ci}D_o/U_o$ can be discerned which is the result of the finite lip thickness and resulting wake instability. By further decreasing r_u to 1 (Fig. 8g), the ISL instability becomes negligible and wake instability governs the inner mixing layer. However, as can be observed, the traces of $\bar{\Lambda}_{ci}D_o/U_o$ as a result of the wake instability do not extend far downstream indicating

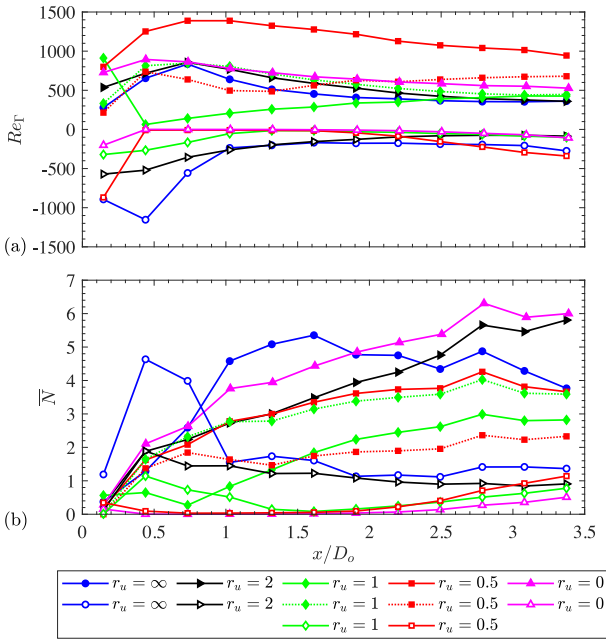


Fig. 9. Axial variation of the normalized vortex strength and the number of detected vortices for different r_u . Filled symbols denote +ve sign vortices. For $r_u = 1$ and 0.5, filled symbols connected by solid and dotted lines denote +ve sign vortices detected in the ISL and OSL, respectively. Open symbols denote -ve sign vortices.

that the generated wake vortices dissipate or break-up fast. At $r_u = 0.5$ (Fig. 8h), the trace of +ve sign $\bar{\Lambda}_{ci} D_o / U_o$ associated with the ISL is much more distinct than the one associated with the OSL, suggesting that the vortices in the ISL do not dissipate or break-up as fast as those in the OSL. We will next discuss the strengths of the vortices and their numbers as a function of the downstream distance from the nozzle.

4.2. Vortex strengths and numbers

The determined vortex Reynolds numbers, $Re_F = \Gamma/\nu$, where ν denotes the kinematic fluid viscosity ($\nu = 15.6 \times 10^{-6} \text{ m}^2/\text{s}$ at 26°C), and the average number of the detected vortex cores in a bin, \bar{N} , were evaluated for streamwise bin sizes of $\Delta x/D_o = 0.3$ (for smaller bin sizes the data were not converged). Results are plotted in Fig. 9 as a function of the distance from the nozzle exit for all investigated r_u . Note that Re_F represents the average strength of a vortex core residing in a certain bin (i.e. at a certain downstream position). For $r_u = 1$ and 0.5, +ve sign vortices associated with the ISL ($r/D_o < 0.35$), and the OSL ($r/D_o \geq 0.35$) were detected separately and are denoted by filled symbols connected by a solid and dotted line, respectively, while -ve sign vortices are presented as open symbols connected by solid lines (see Fig. 9).

Except for $r_u = \infty$ (when $x/D_o \leq 1$), it can be observed that values of $|Re_F|$ and \bar{N} associated with the -ve sign vortices are in all cases smaller than the values associated with the +ve sign vortices. The -ve sign vortices are generated in the inner shear layer governed by the velocity jump, $|\Delta U_i|$, which equals $U_o/2$, 0 and U_o for $r_u = 2$, 1 and 0.5, respectively. Note that for $r_u = 0.5$, ΔU_i and ΔU_o have the same sign and magnitude, and as a result between $0.5 < x/D < 3$, no -ve sign vortices are generated. Beyond $x/D = 3$ they increasingly appear (Fig. 9b) likely due to fragmentation of the large toroidal vortices and rearrangement of the vorticity due to the strain rate acting on it. As r_u is increased, -ve sign vortices become more abundant (Fig. 9b). For $r_u = 1$, the inner shear layer is governed by wake instability, and results indicate that close to the nozzle exit, -ve sign vortices exist (Fig. 9b).

They disappear within $1.5 < x/D_o < 1.8$ illustrating the limited extent of the wake instability at this r_u .

For $r_u = \infty$ (annular jet), strong -ve sign vortices are generated close to the exit of the nozzle ($0.3 < x/D_o < 0.6$). Their magnitude ($|Re_F|$) is about twice that of the +ve sign vortices in the OSL at the same axial locations (Fig. 9a), and their average number per bin (Fig. 9b) is more than twice as high when $x/D_o \leq 0.6$. In agreement with the contracting annular jet and the “closed” recirculating region for this r_u (see Fig. 4), the -ve sign vortices either do not “leave” the recirculating region or are broken up into small fragments and \bar{N} as well as $|Re_F|$ strongly decrease beyond $x/D_o \approx 0.6$.

It is interesting to note that for $r_u = \infty$, 2, 1, and 0, despite differences in vortex strength up till $x/D_o \approx 1.5$, values of Re_F associated with the +ve sign vortices in the OSL converge to a similar value at $x/D_o \approx 3.4$ (Fig. 9a). Note that for both $r_u = 0.5$ and 1, the number of ISL +ve sign vortices strongly exceeds that in the OSL (Fig. 9b). However, for $r_u = 0.5$, values of Re_F for +ve sign vortices in the ISL exceed those of the other investigated r_u while values of Re_F for +ve sign vortices in the OSL converge to similar Re_F (at $x/D_o \approx 3.4$) as those of the other investigated r_u . This is in agreement with the ensemble averaged swirling strength maps depicted in Fig. 8h that clearly indicate that the inner shear layer vortices are strongest. The most obvious reason for this is that the inner shear layer vortex generation is not dictated by $\Delta U_i = U_o$ (for $r_u = 0.5$), but instead by $\Delta U_i \sim 2U_o$, i.e. the effect of the outer jet is negligible as it merges quickly with the inner jet (Fig. 6). After merging, the shear rate is much enhanced resulting in the generation of stronger +ve sign vortices in the ISL. Note that our results show that in all other cases, $\Delta U_o = U_o$ dictates the +ve sign vortex generation.

4.3. Instantaneous vorticity and swirling strength distributions

More insight into the vortex generation and their interaction due to wake and shear layer instabilities can be obtained by further analyzing the instantaneous vorticity and swirling strength distributions. Example snapshots of $\omega D_o / U_o$ and $\Lambda_{ci} D_o / U_o$ are depicted in Figs. 10 to 13 for $r_u = \infty$, 2, 1, and 0.5, respectively. In agreement with the distribution of $\bar{\Lambda}_{ci} D_o / U_o$ (Fig. 8e), the instantaneous snapshots depicted in Fig. 10 for $r_u = \infty$ clearly show that the -ve sign vortices in the ISL are generated almost immediately as the outer jet leaves the annulus. Furthermore, these -ve sign vortices are mostly recirculated within the recirculation region (see for example Fig. 10a). However, occasionally the recirculating wake “opens up” and -ve sign vortices may escape (Fig. 10b) explaining why \bar{N} does not decrease to zero for $x/D_o > 1$ (Fig. 9b).

When r_u decreases from ∞ to 2 (Fig. 11), the recirculating wake disappears (see Fig. 4) and the ISL stretches in the downstream direction as previously shown in the ensemble averaged vorticity and swirling strength distributions (Fig. 8). The instantaneous snapshots of the vorticity and the swirling strength at $r_u = 2$ (Fig. 11) confirm this. Close to the nozzle exit, the vorticity plots (upper row in Fig. 11) exhibit three vorticity “layers” associated with the three boundary layers that developed inside the nozzle. Contour plots of $\Lambda_{ci} D_o / U_o$ (bottom row in Fig. 11) show that near the nozzle exit, combined wake and shear instabilities (the latter are likely to govern at $r_u = 2$) lead to the generation of +ve and -ve sign vortex pairs in the ISL, of which only the -ve sign vortices are advected downstream as their strength diminishes (see Figs. 9a and 11). This is in agreement with the ensemble averaged swirling strength traces (Fig. 8f). Similar as for $r_u = \infty$, the +ve sign vortices associated with the OSL roll up at a later stage ($x/D_o \approx 0.2$ – 0.3) due to K-H instabilities. Clearly, planar signatures of toroidal vortices can be discerned illustrated by the pairs of swirling strength blobs at the periphery of the coaxial jet. Note that although in many cases, the blobs are “in-line” arranged (at the same x/D_o position, see +ve sign “blobs” in dashed ellipse in Fig. 11h), especially close to the nozzle ($x/D_o \approx 1$), also “staggered” (pair of +ve sign “blobs”

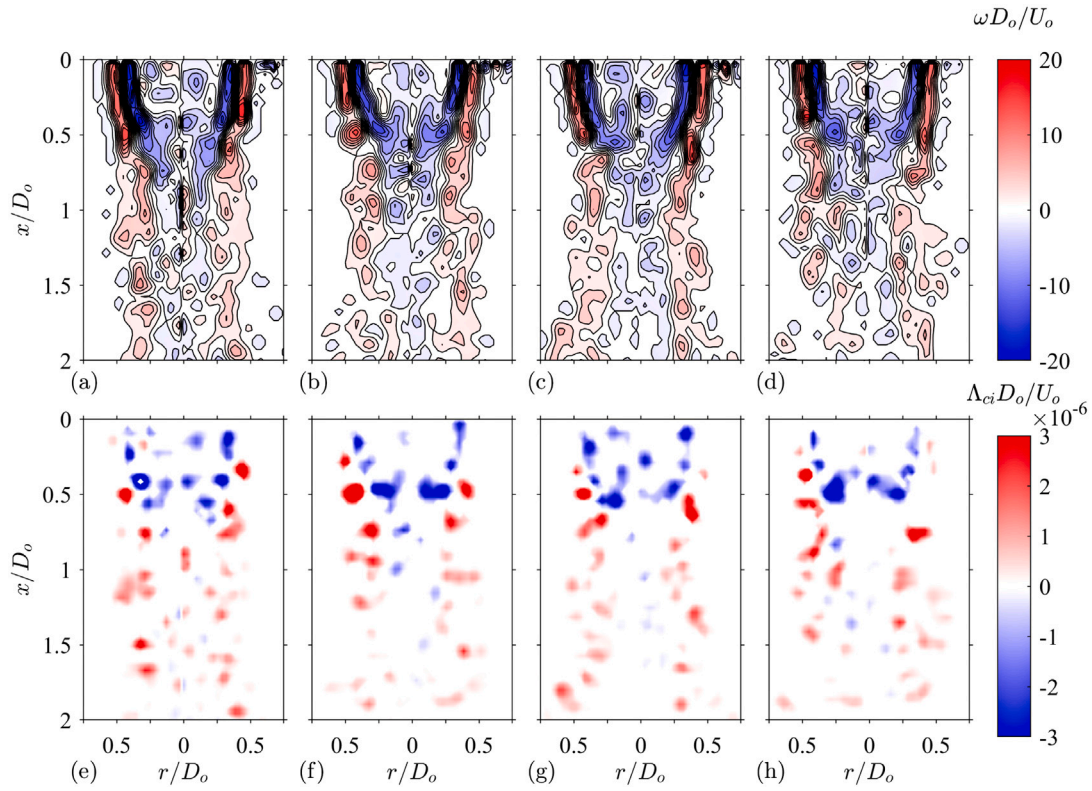


Fig. 10. Examples snapshot contour plots of the instantaneous vorticity (upper row) and the associated swirling strength (bottom row), $r_u = \infty$.

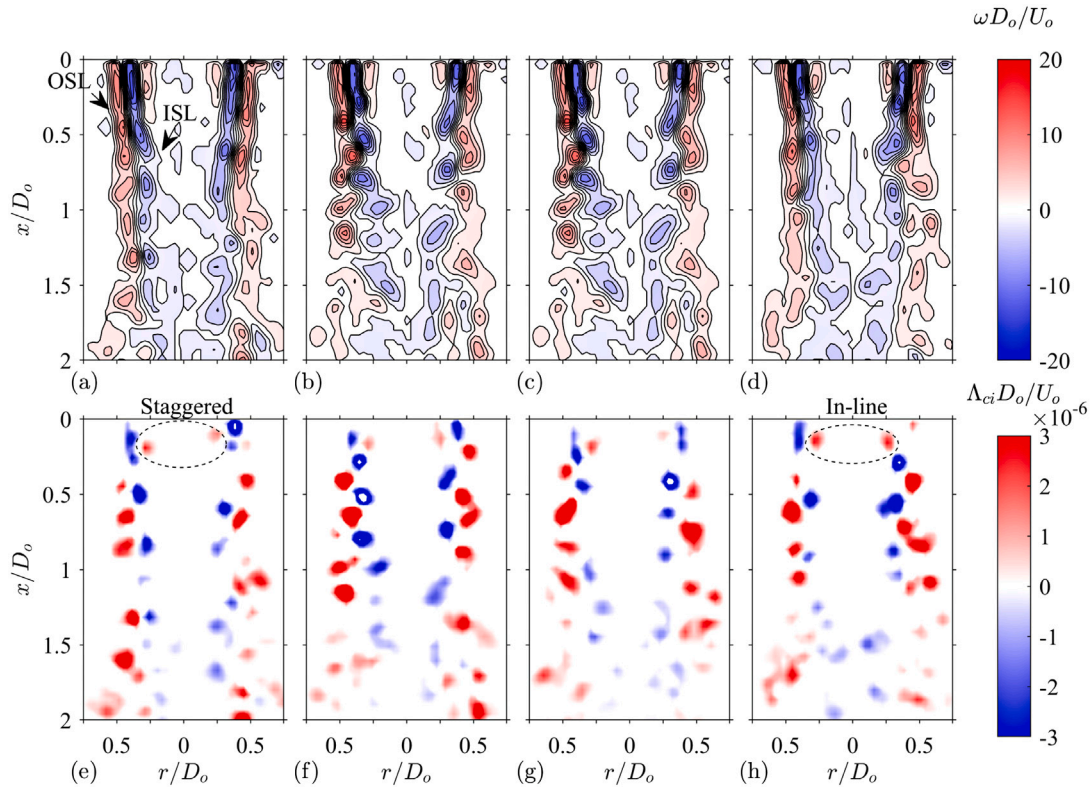


Fig. 11. Examples snapshot contour plots of the instantaneous vorticity (upper row) and the associated swirling strength (bottom row), $r_u = 2$.

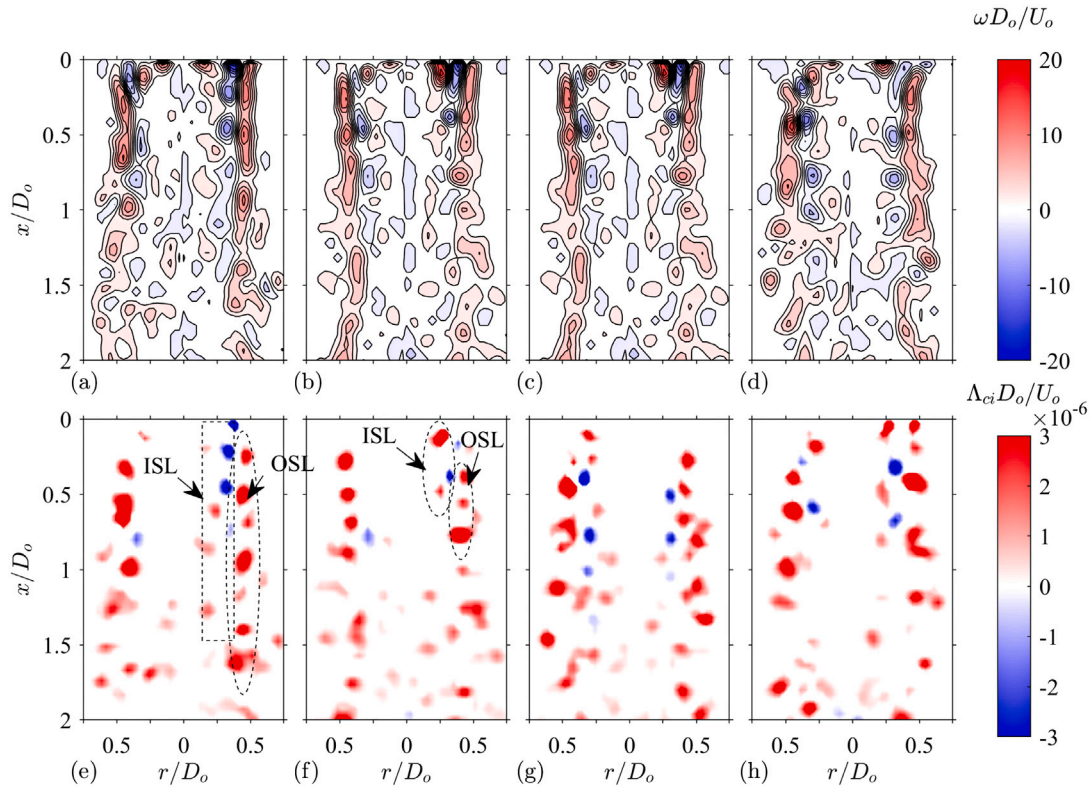


Fig. 12. Examples snapshot contour plots of the instantaneous vorticity (upper row) and the associated swirling strength (bottom row), $r_u = 1$.

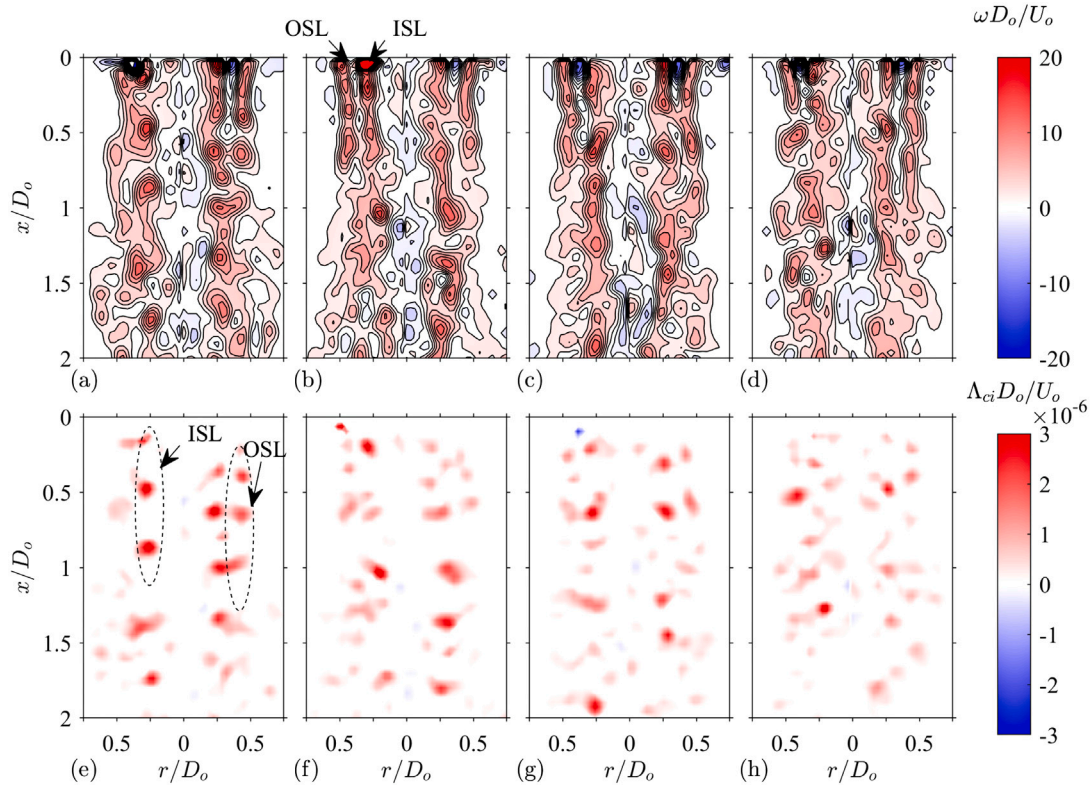


Fig. 13. Examples snapshot contour plots of the instantaneous vorticity (upper row) and the associated swirling strength (bottom row), $r_u = 0.5$.

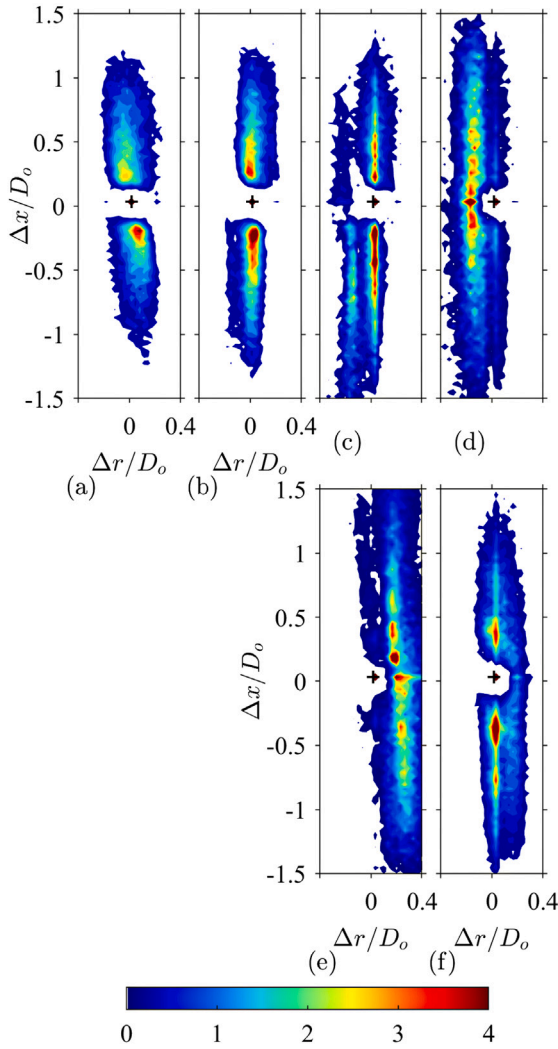


Fig. 14. JPDFs of the +ve sign vortices (“nearest neighbors”) with respect to the strongest, reference +ve sign vortex. Upper and bottom rows depict vortices in the outer and inner layer, respectively. r_u = (a) ∞ , (b) 2, (c) 1, and (d, e) 0.5. Black “+” symbol at (0, 0) denotes the location of the reference (strongest) vortex.

in dashed ellipse in Fig. 11f) configurations are observed hinting at helical vortex shedding (see Fig. 11). This observation is similar to that reported for a single, round jet by Corke et al. (1991). They showed that the flow switches randomly from axisymmetric (inline) to helical (staggered) vortex shedding, suggesting a strong dependence on the instantaneous initial conditions at the lip of the nozzle(s).

At $r_u = 1$ (Fig. 12), the instantaneous snapshots of vorticity and the directional swirling strength show clear signs of both wake and shear layer instabilities. In contrast to $r_u = 2$ (Fig. 11), now “trains” of +ve and -ve sign vortices are observed in the ISL. These are the result of the wake instability due to the finite wall thickness. However, even for this r_u , the -ve sign vortices are not detected for $1.2 < x/D_o < 2.1$ (Fig. 9b) (see also the average swirling strength plots in Fig. 8). It is clear from the instantaneous snapshots that the +ve sign vortices in the OSL are stronger than those generated by the wake instability in the ISL, and they form distinct, coherent trains of equally spaced vortices as will be further discussed in the next section.

For $r_u = 0.5$ (Fig. 13), the velocity jumps in the ISL and the OSL are equal and have the same sign, i.e. $\Delta U_i = \Delta U_o = U_o$. As a result, +ve sign vortices govern both the ISL and the OSL (see Fig. 13). Note that -ve sign vortices are absent near the nozzle exit (see also Fig. 9b). Distinct, strong +ve sign vortices are observed in both the OSL and the

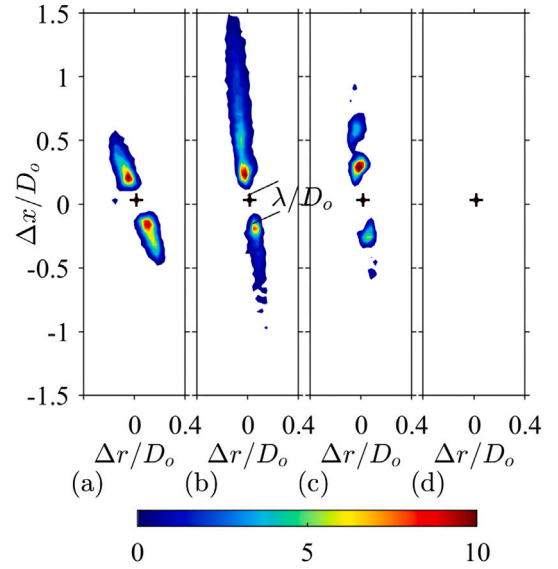


Fig. 15. JPDFs of the -ve sign vortices (“nearest neighbors”) with respect to the strongest, reference -ve sign vortex. r_u = (a) ∞ , (b) 2, (c) 1, and (d) 0.5. Black “+” symbol at (0, 0) denotes the location of the reference (strongest) vortex.

ISL (bottom row of Fig. 13). However, the mean swirling strength maps for this r_u (Fig. 8) as well as the axial distribution of Re_T (Fig. 9a) indicate that the inner layer’s vortices are on average stronger and more coherent than those in the OSL. Note that these results are different than the visualizations by Dahm et al. (1992) at $r_u = 0.59$. They showed that in their case, the inner layer is dynamically irrelevant and that the near-field appears to be dominated by the outer layer. This difference may be due to different flow exit conditions which were laminar in the experiments performed by Dahm et al. (1992).

4.4. Spatial organization and Strouhal numbers

The instantaneous swirling strength snapshots can be analyzed in order to extract the spatial organization of the generated vortices near the nozzle exit, and to estimate the wavelength of the primary instability as a result of K-H instabilities. Since our measurements were not time resolved and represent an ensemble of statistically independent vector maps, the following approach was taken. First, the strongest +ve and -ve sign vortices were detected within the range $0.12 < x/D_o < 1.8$ for each instantaneous vector map. Note that for $r_u = 0.5$ and 1 (see Figs. 12 and 13), the strongest +ve sign vortices were detected separately in the ISL ($r/D_o < 0.35$) and OSL ($r/D_o \geq 0.35$). In general, the reference +ve sign vortices were detected farther downstream than the strongest -ve sign vortices.

In order to characterize the spatial vortex organization close to the nozzle exit, the detected strongest +ve sign vortices were taken as reference and the relative positions ($\Delta x/D_o, \Delta r/D_o$) of adjacent +ve sign vortices (termed as “nearest neighbors”) were determined. The same was done for the -ve sign vortices and the joint probability density functions (JPDFs) of the positions of the “nearest neighbors” with respect to the reference +ve and -ve sign vortices are depicted in Figs. 14 and 15, respectively, for all investigated r_u . As expected from the instantaneous vorticity and swirling strength maps depicted in Figs. 10 to 13, the JPDFs indicate well-organized patterns of nearest neighbors about the strongest reference vortices. The obtained JPDFs are nearly symmetric about the origin in agreement with the instantaneous sequences of coherent, same sign vortices generated in the shear layers (Figs. 10 to 13). Note that for $r_u = 0.5$, a negligible number of -ve sign vortices were detected (Fig. 15d). The distance of the highest probability peak to the origin represents the normalized,

primary instability wavelength, λ/D_o (see Fig. 15b). Estimated values of λ/D_o are summarized in Table 2. Values for the +ve sign (subscript “+”) and –ve sign (subscript “–”) vortices were determined in each layer (denoted by superscripts “i”, “io” and “o”, see Fig. 1) associated within the ISL and OSL. As can be seen in Table 1, values range between $0.2 < \lambda/D_o < 0.39$. Note that these values are smaller than in Au and Ko (1987) who reported values of $\lambda_o/D_o = 0.4$ at $x/D_o = 0.4$ increasing to $\lambda_o/D_o = 1.8$ at $x/D_o = 3$. We surmise that this discrepancy is the result of differences in nozzle geometry and Reynolds numbers.

Assuming vortex convection velocities that equal $U_{c,i} = (U_i + U_o)/2$ and $U_{c,o} = 0.6U_o$ (Ko and Kwan, 1976; Popiel and Trass, 1991) in the ISL and OSL, respectively, estimates of vortex shedding frequencies, f , can be obtained. Associated Strouhal numbers, $St = f l/U$, that represent the vortex shedding frequencies normalized by a characteristic length, l , and characteristic velocity, U , can be determined. In Table 2, Strouhal numbers based on the wall thickness, St_i , the momentum thickness, St_θ , and the inner or outer nozzle diameter, St , are summarized.

A comparison of the present Strouhal numbers to those in the literature (Ko and Kwan, 1976; Segalini and Talamelli, 2011) reveals that the present values are higher. For example, Ko and Kwan (1976) reported that St based on D_o and U_o in the initial merging zone (for $r_u = 0.3, 0.5$, and 0.7) did not exceed 1, and values corresponded well to those obtained for a single jet. In contrast, the present estimated values of St exceed 1 in all cases with maximum values exceeding 3 (Table 2). Based on θ , Segalini and Talamelli (2011) showed that $St_i^t (= f \theta^i/U_i)$ is nearly constant for $r_u < 0.75$ and approaches the value observed for a single jet for small r_u ($St \approx 0.012$, Zaman and Hussain (1980), laminar jet exit boundary layers). Similarly, they found that $St_{\theta o}$ ranged between $0.01 < St_{\theta o} < 0.015$ for $1 < r_u < 2$ and approaches $St_{\theta o} \approx 0.013$ for large r_u . In addition, they reported values of St_i that were much smaller than the ones reported in the present research. This discrepancy is puzzling and we surmise that it may be the result of several reasons. First, both Ko and Kwan (1976) as well as Segalini and Talamelli (2011) used a contracting nozzle in contrast to the present nozzle geometry where the inner jet was issued from a long tube. As a result, in the present case, turbulence levels at the jet exit were much higher (Fig. 7) which may lead to different excitation of existing instabilities in the near-field. Secondly, the area ratio used by Ko and Kwan (1976) and Segalini and Talamelli (2011) was $A_o/A_i \approx 3$ while in the present research $A_o/A_i = 1$. As a result, h is much smaller in the present case and interaction between the inner and outer shear layers is expected to occur (note that $\delta_{\omega} \sim h$, Table 1). Third, Buresti et al. (1994) showed that with increasing axial distance from the jet exit, St numbers decreased. This is in agreement with results for a single round jet reported by Popiel and Trass (1991) who showed that $St = 1.2(x/D)^{-1}$. In the present case, St were determined in the immediate vicinity of the jet exit ($x/D_o \approx 1$) and are expected to be higher than one in this region. In order to corroborate our results, we estimated the Strouhal numbers in the visualizations by Dahm et al. (1992) assuming the same vortex convection velocities. The estimates are $St_+^o \approx 2.8, 1.5$, and 6.7 for $r_u = 0.59, 1$, and 2.56 , respectively, i.e. of the same order of magnitude as those reported in Table 2 for similar r_u . Another fourth reason that may explain the discrepancy is the vortex convection velocity that may be taken too low close to the nozzle exit.

The JPFDs depicted in Figs. 14 and 15 depict the relative spatial organization of same sign vortices. However, for $r_u = \infty, 2$, and 1 , both –ve and +ve sign vortices were generated close to the nozzle exit and it is of interest to look at the relative position of +ve sign and –ve sign vortices. JPFDs of the relative position of the –ve sign vortices with respect to the strongest +ve sign vortex and vice versa are depicted in the upper and lower rows of Fig. 16, respectively. A clear “staggered” pattern is observed for $r_u = 2$ (Figs. 16b,e) in agreement with the instantaneous swirling strength maps presented in Fig. 11. For $r_u = 1$ (right column in Fig. 16), also clear spatial patterns can be observed. The pattern with respect to the reference –ve sign vortex (Fig. 16f) is staggered and indicates clear trains of ISL and OSL +ve sign vortices.

Table 2

Normalized, primary, spatial instability wavelengths associated with the three interfaces (Fig. 1) denoted by the superscripts “i”, “io” and “o”, for all investigated r_u . Note that the subscripts “+” and “–” denote “associated with +ve and –ve sign vortices, respectively.”

r_u	0.5	1	2	∞
λ_+^i/D_o	0.39	0.31	–	–
λ_-^i/D_o	–	0.28	0.21	0.20
λ_+^o/D_o	0.21	0.21	0.25	0.22
$U_{c,i} (= (U_i + U_o)/2)$ [m/s]	44.1	29.4	22.0	14.7
$U_{c,o} (= U_o)$ [m/s]	17.6	17.6	17.6	17.6
$St_+^i (= f_+^i D_i/U_i)$	1.15	1.94	–	–
$St_-^i (= f_-^i D_o/U_o)$	–	3.57	3.57	2.50
$St_+^o (= f_+^o D_o/U_o)$	2.73	2.40	2.86	2.86
$St_{i,+}^t (= f_+^i t/U_{c,i})$	0.26	0.32	–	–
$St_{i,-}^t (= f_-^i t/U_{c,i})$	–	0.36	0.48	0.50
$St_{\theta,+}^t (= \theta^i f_+^i/U_i)$	0.071	0.126	–	–
$St_{\theta,+}^t (= \theta^o f_+^o/U_o)$	0.082	0.065	0.080	0.071

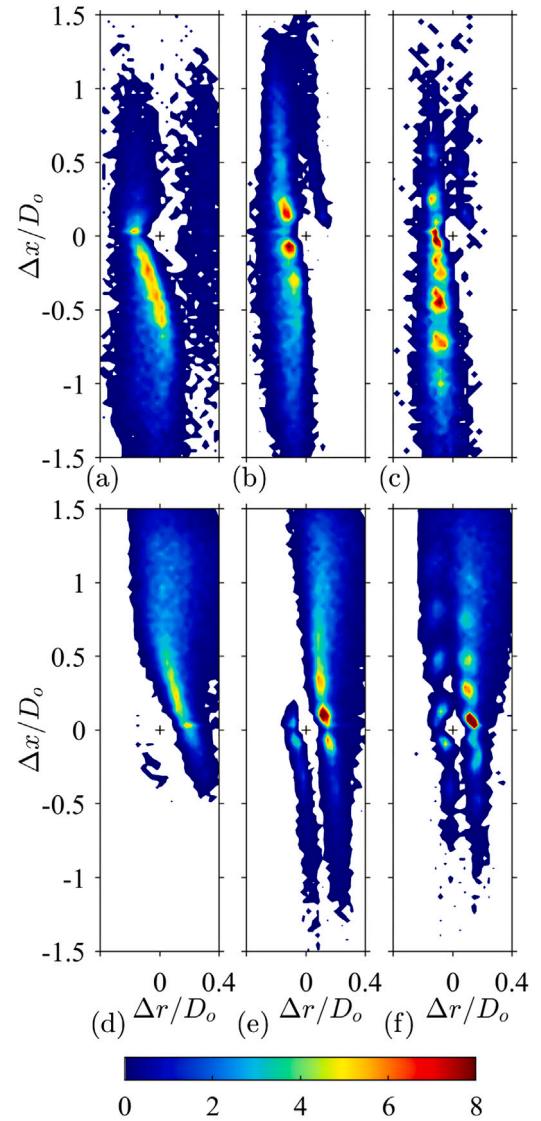


Fig. 16. JPFDs of positions of –ve sign vortices with respect to the reference +ve sign vortex (upper row) and vice versa (bottom row). $r_u = (a), (d) \infty, (b,e) 2, (c,f) 1$.

Note that especially in the OSL, the sequence is highly repetitive and high probability peaks can be discerned up till $\Delta x/D_o \approx 1$ (Fig. 16f). Further downstream, relative to the reference +ve sign vortex in the OSL (Fig. 16c), the -ve sign vortices are preferably inline aligned with it, as indicated by the repetitive sequence of -ve sign vortices in the JPDF (Fig. 16c) upstream of the reference vortex position. These results clearly show that the two shear layers do not develop independently and vortex generation seems to be governed by lock-in between the layers. Note that this can also be expected since the vorticity thickness (see Table 1) associated with the three shear layers at the jet exit are of the order of the gap width, h .

5. Summary and conclusions

In this research, we presented detailed planar PIV measurements of the flow field characteristics in the near-field of a coaxial air jet. Measurements were performed at $r_u = \infty, 2, 1$, and 0.5 while keeping U_o constant. As baseline reference, the flow field of a single jet ($r_u = 0$) was also measured. The inner jet was issued from a long tube while the outer jet was issued from a contracting nozzle. The axial and radial mean velocity distributions were typical of coaxial jets, and compared well to those reported in the literature. For $r_u = \infty$, the jet strongly contracted and a recirculating region was observed close to the jet exit. As r_u was decreased, the inner jet became increasingly important and for $r_u = 0.5$, it dominated the downstream flow field.

In this research, we were especially interested in the strength, numbers, and spatial organization of the generated vortices in the near-field of the jet. Based on the instantaneous vorticity and swirling strength distributions, the vortex strengths, and their numbers were analyzed. Instantaneous vorticity and swirling strength distributions revealed different vortex generation patterns for the different r_u . In all cases, +ve sign vortices generated as a result of positive velocity jumps, dominated the flow field. Only for $r_u = 2$, -ve sign vortices (as a result of a negative velocity jump, $\Delta U_i = -U_o$) persisted downstream. At $r_u = \infty$, strong -ve sign vortices were observed close to the nozzle exit in the recirculating flow region. They were only sparsely detected beyond the recirculation region. For $r_u = \infty, 2$, and 1 , +ve sign vortices in the OSL dominated the downstream flow field. However, somewhat surprisingly at $r_u = 0.5$, the +ve sign vortices in the ISL dominated the downstream flow field likely because the outer jet quickly merges with the inner one and the “effective” velocity jump is strongly enhanced.

The spatial organization of the generated vortices was elucidated by determining the relative positions of vortices adjacent to assigned reference vortices. This analysis revealed distinct spatial wavelengths of the generated vortices in the ISL and OSL. Associated Strouhal numbers (assuming vortex convection velocities) were higher than those reported in the literature at similar r_u but different nozzle geometry. This points at a strong effect of nozzle geometry on the vortex generation frequency. Furthermore, our results indicated that for the present nozzle geometry ($A_o/A_i = 1$) and jet exit flow conditions, the outer and inner jet do not develop independently but are strongly coupled.

CRedit authorship contribution statement

A. Mitra: Methodology, Software, Validation, Formal analysis, Investigation, Data curation, Writing – original draft, Writing – review & editing, Visualization. **S. Murugan:** Methodology, Software, Validation, Formal analysis, Investigation, Data curation, Writing – original draft, Writing – review & editing, Visualization. **R. van Hout:** Conceptualization, Writing – original draft, Writing – review & editing, Visualization, Funding acquisition, Project administration. **A. Kleiman:** Investigation, Methodology, Resources, Project administration. **M. Raizner:** Conceptualization, Supervision, Project administration, Funding acquisition. **B. Cukurel:** Conceptualization, Writing – review & editing, Funding acquisition, Project administration.

Declaration of competing interest

The authors declare that they have no known competing financial interests or personal relationships that could have appeared to influence the work reported in this paper.

Data availability

Data will be made available on request.

Acknowledgments

This research was funded by the Pazy Foundation and supported in part at the Technion by the Zeff Fellowship. The authors acknowledge the financial support of Minerva Research Center for Micro Turbine Powered Energy Systems (Max Planck Society Contract AZ5746940764).

References

- Adrian, R.J., Christensen, K.T., Liu, Z.C., 2000. Analysis and interpretation of instantaneous turbulent velocity fields. *Exp. Fluids* 29 (3), 275–290. <http://dx.doi.org/10.1007/s003489900087>.
- Adrian, R.J., Westerweel, J., 2011. *Particle Image Velocimetry*. Cambridge University Press, p. 558.
- Akselvoll, K., Moin, P., 1996. Large-eddy simulation of turbulent confined coannular jets. *J. Fluid Mech.* 315, 387–411.
- Au, H., Ko, N., 1987. Coaxial jets of different mean velocity ratios, part 2. *J. Sound Vib.* 116 (3), 427–443. [http://dx.doi.org/10.1016/S0022-460X\(87\)81375-5](http://dx.doi.org/10.1016/S0022-460X(87)81375-5).
- Balarac, G., Métais, O., 2005. The near field of coaxial jets: A numerical study. *Phys. Fluids* 17 (6), 065102. <http://dx.doi.org/10.1063/1.1900786>.
- Balarac, G., Métais, O., Lesieur, M., 2007a. Mixing enhancement in coaxial jets through inflow forcing : a numerical study. *Phys. Fluids* <http://dx.doi.org/10.1063/1.2747680>.
- Balarac, G., Si-Ameur, M., Si-Ameur, M., Si-Ameur, M., Lesieur, M., Métais, O., 2007b. Direct numerical simulations of high velocity ratio coaxial jets: mixing properties and influence of upstream conditions. *J. Turbul.* <http://dx.doi.org/10.1080/14685240600833094>.
- Ball, C., Fellouah, H., Pollard, A., 2012. The flow field in turbulent round free jets. *Prog. Aerosp. Sci.* 50, 1–26.
- Benedict, L.H., Gould, R.D., 1996. Towards better uncertainty estimates for turbulence statistics. *Exp. Fluids* 22 (2), 129–136. <http://dx.doi.org/10.1007/s003480050030>.
- Buresti, G., Petagna, P., Talamelli, A., 1998. Experimental investigation on the turbulent near-field of coaxial jets. *Exp. Therm Fluid Sci.* 17 (1–2), 18–26. [http://dx.doi.org/10.1016/S0894-1777\(97\)10045-0](http://dx.doi.org/10.1016/S0894-1777(97)10045-0).
- Buresti, G., Talamelli, A., Petagna, P., 1994. Experimental characterization of the velocity field of a coaxial jet configuration. *Exp. Therm Fluid Sci.* 9 (2), 135–146. [http://dx.doi.org/10.1016/0894-1777\(94\)90106-6](http://dx.doi.org/10.1016/0894-1777(94)90106-6).
- Canton, J., Auteri, F., Carini, M., 2017. Linear global stability of two incompressible coaxial jets. *J. Fluid Mech.* 824, 886–911. <http://dx.doi.org/10.1017/jfm.2017.290>.
- Chakraborty, P., Balachandar, S., Adrian, R.J., 2005. On the relationships between local vortex identification schemes. *J. Fluid Mech.* 535, 189–214.
- Champagne, F.H., Kromat, S., 2000. Experiments on the formation of a recirculation zone in swirling coaxial jets. *Exp. Fluids* 29 (5), 494–504. <http://dx.doi.org/10.1007/s003480000118>.
- Champagne, F., Wygnanski, I.J., 1971. An experimental investigation of coaxial turbulent jets. *Int. J. Heat Mass Transfer* 14 (9), 1445–1464. [http://dx.doi.org/10.1016/0017-9310\(71\)90191-8](http://dx.doi.org/10.1016/0017-9310(71)90191-8).
- Chigier, N.A., Beér, J.M., 1964. The Flow Region near the nozzle in double concentric jets. *J. Basic Eng.* 86 (4), 797–804. <http://dx.doi.org/10.1115/1.3655957>.
- Cohen, J., Wygnanski, I., 1987. The evolution of instabilities in the axisymmetric jet. Part 1. The linear growth of disturbances near the nozzle. *J. Fluid Mech.* 176, 191–219. <http://dx.doi.org/10.1017/S0022112087000624>.
- Corke, T.C., Shakib, F., Nagib, H.M., 1991. Mode selection and resonant phase locking in unstable axisymmetric jets. *J. Fluid Mech.* 223, 253–311. <http://dx.doi.org/10.1017/S0022112091001428>.
- Dahm, W.J.A., Frier, C.E., Tryggvason, G., 1992. Vortex structure and dynamics in the near field of a coaxial jet. *J. Fluid Mech.* 241, 371–402. <http://dx.doi.org/10.1017/S0022112092002088>.
- Duraõ, D., Whitelaw, J., 1973. Turbulent mixing in the developing region of coaxial jets. *J. Fluids Eng.* <http://dx.doi.org/10.1115/1.3447051>.
- Gladnick, P., Enotiadis, A., LaRue, J., Samuelsen, G., 1990. Near-field characteristics of a turbulent coflowing jet. *AIAA J.* 28 (8), 1405–1414.
- Kadu, P.A., Sakai, Y., Ito, Y., Iwano, K., Sugino, M., Katagiri, T., Hayase, T., Nagata, K., 2020. Application of spectral proper orthogonal decomposition to velocity and passive scalar fields in a swirling coaxial jet. *Phys. Fluids* 32 (1), 015106. <http://dx.doi.org/10.1063/1.5131627>.

- Ko, N., Au, H., 1981. Initial region of subsonic coaxial jets of high mean-velocity ratio. *J. Fluids Eng.* 103, 335–338. <http://dx.doi.org/10.1115/1.3241742>.
- Ko, N., Au, H., 1985. Coaxial jets of different mean velocity ratios. *J. Sound Vib.* 100 (2), 211–232. [http://dx.doi.org/10.1016/0022-460X\(85\)90416-X](http://dx.doi.org/10.1016/0022-460X(85)90416-X).
- Ko, N., Kwan, A., 1976. The initial region of subsonic coaxial jets. *J. Fluid Mech.* 73 (2), 305–332. <http://dx.doi.org/10.1017/S0022112076001389>.
- Kwan, S.h., 1975. Noise Mechanisms in the Initial Region of Coaxial Jets (Degree Thesis of the University of Hong Kong). Hong Kong university.
- Kwan, A., Ko, N., 1976. Coherent structures in subsonic coaxial jets. *J. Sound Vib.* 48 (2), 203–219. [http://dx.doi.org/10.1016/0022-460X\(76\)90460-0](http://dx.doi.org/10.1016/0022-460X(76)90460-0).
- Michalke, A., 1984. Survey on jet instability theory. *Prog. Aerosp. Sci.* 21, 159–199. [http://dx.doi.org/10.1016/0376-0421\(84\)90005-8](http://dx.doi.org/10.1016/0376-0421(84)90005-8).
- Montagnani, D., Auteri, F., 2019. Non-modal analysis of coaxial jets. *J. Fluid Mech.* 872, 665–696. <http://dx.doi.org/10.1017/jfm.2019.356>.
- Popiel, C.O., Trass, O., 1991. Visualization of a free and impinging round jet. *Exp. Therm Fluid Sci.* 4 (3), 253–264. [http://dx.doi.org/10.1016/0894-1777\(91\)90043-Q](http://dx.doi.org/10.1016/0894-1777(91)90043-Q).
- Raizner, M., Rinsky, V., Grossman, G., Van Hout, R., 2019a. The effect of jet pulsation on the flow field of a round impinging jet and the radially expanding wall jet. *Int. J. Heat Mass Transfer* 140, 606–619.
- Raizner, M., Rinsky, V., Grossman, G., van Hout, R., 2019b. Heat transfer and flow field measurements of a pulsating round jet impinging on a flat heated surface. *Int. J. Heat Fluid Flow* 77, 278–287.
- Raizner, M., Rinsky, V., van Hout, R., Grossman, G., 2018. Heat transfer and flow field measurements of a pulsating round jet impinging on a flat heated surface. In: *Proceedings of the 9th Symposium of Turbulence, Heat and Mass Transfer. THMT 2018*, July 10–13, Rio de Janeiro, Brasil, Begell-House Inc., New-York.
- Raizner, M., van Hout, R., 2020. Effect of impinging jet pulsation on primary and secondary vortex characteristics. *Int. J. Heat Mass Transfer* 151, 119445.
- Rajaratnam, N., 1976. *Turbulent Jets*. Elsevier.
- Rehab, H., Villermaux, E., Hopfinger, E., 1997. Flow regimes of large-velocity-ratio coaxial jets. *J. Fluid Mech.* 345, 357–381. <http://dx.doi.org/10.1017/S002211209700637X>.
- Ribeiro, M., Whitelaw, J., 1976. Turbulent mixing of coaxial jets with particular reference to the near-exit region.
- Ribeiro, M., Whitelaw, J., 1980. Coaxial jets with and without swirl. *J. Fluid Mech.* 96 (4), 769–795. <http://dx.doi.org/10.1017/S0022112080002352>.
- Sadr, R., Klewicki, J.C., 2003. An experimental investigation of the near-field flow development in coaxial jets. *Phys. Fluids* 15 (5), 1233–1246. <http://dx.doi.org/10.1063/1.1566755>.
- Schlichting, H., Kestin, J., 1961. *Boundary Layer Theory*, Vol. 121. Springer.
- Segalini, A., Talamelli, A., 2011. Experimental analysis of dominant instabilities in coaxial jets. *Phys. Fluids* 23 (2), 024103. <http://dx.doi.org/10.1063/1.3553280>.
- da Silva, C.B., Balarac, G., Métais, O., 2003. Transition in high velocity ratio coaxial jets analysed from direct numerical simulations. *J. Turbul.* 4, N24. <http://dx.doi.org/10.1088/1468-5248/4/1/024>.
- Talamelli, A., Gavarini, I.M., 2006. Linear instability characteristics of incompressible coaxial jets. *Flow Turbul. Combust.* <http://dx.doi.org/10.1007/s10494-006-9015-9>.
- van Hout, R., Murugan, S., Mitra, A., Cukurel, B., 2021. Coaxial circular jets—A review. *Fluids* 6 (4), 147.
- van Hout, R., Rinsky, V., Grobman, Y.G., 2018. Experimental study of a round jet impinging on a flat surface: flow field and vortex characteristics in the wall jet. *Int. J. Heat Fluid Flow* 70 (January), 41–58. <http://dx.doi.org/10.1016/j.ijheatfluidflow.2018.01.010>.
- van Hout, R., Sabban, L., Cohen, A., 2013. The use of high-speed PIV and holographic cinematography in the study of fiber suspension flows. *Acta Mech.* 224 (10), 2263–2280.
- Villermaux, E., Rehab, H., 2000. Mixing in coaxial jets. *J. Fluid Mech.* 425, 161–185.
- Violato, D., Ianiro, A., Cardone, G., Scarano, F., 2012. Three-dimensional vortex dynamics and convective heat transfer in circular and chevron impinging jets. *Int. J. Heat Fluid Flow* 37, 22–36. <http://dx.doi.org/10.1016/j.ijheatfluidflow.2012.06.003>.
- Westerweel, J., Scarano, F., 2005. Universal outlier detection for PIV data. *Exp. Fluids* 39 (6), 1096–1100.
- Wicker, R.B., Eaton, J.K., 1994. Near field of a coaxial jet with and without axial excitation. *AIAA J.* 32 (3), 542–546. <http://dx.doi.org/10.2514/3.12019>.
- Zaman, K., Hussain, A., 1980. Vortex pairing in a circular jet under controlled excitation. Part 1. General jet response. *J. Fluid Mech.* 101 (3), 449–491.
- Zhou, J., Adrian, R.J., Balachandrar, S., Kendall, T., 1999. Mechanisms for generating coherent packets of hairpin vortices in channel flow. *J. Fluid Mech.* 387, 353–396.